Development of a reliable and low cost miniaturized Reaction Wheel System for CubeSat applications

Ricardo Filipe Pereira Gomes

Thesis to obtain the Master of Science Degree in

Aerospace Engineering

Supervisor: Prof. Afzal Suleman

Examination Committee

Chairperson: Prof. Fernando José Parracho Lau
Supervisor: Prof. Afzal Suleman
Member of the Committee: Prof. António Manuel Relógio Ribeiro

April 2016

To my parents and sister for their unconditional support

Acknowledgments

I would like to begin by thanking my supervisor, Dr. Afzal Suleman in particular, who provided this great opportunity that was performing a MSc. thesis in collaboration with the University of Victoria and supervised the whole development of this work. A special thanks goes also to Prof. Fernando Lau (course coordinator) and all the other teachers from the Aerospace Engineering course at IST. Without them passing their knowledge, it would not be possible to reach this stage. I also would like to thank ECOSat team members for providing the topic for my master thesis and which whom I worked during four months. Finally, I would also like to thank my family and specially my mother, Rosa Gomes, who kept believing in me even when I did not believe in myself. I also want to thank all my friends and colleagues for all the support, counselling and friendship provided during my academic path.

Resumo

Actualmente os CubeSats, satélites de pequenas dimensões, requerem sistemas de controlo precisos e rigorosos. De modo a alcançar estes requesitos o uso de rodas de inércia, como componente principal do sistema de controlo, é uma opção a considerar. Esta tese apresenta o desenvolvimento de um sistema de rodas de inércia (SRI) a ser integrado no ECOSat-III, actualmente a ser desenvolvido pela Universidade de Victória. Tal permitirá a criação de uma nova classe de missões actualmente difíceis de alcançar.

É apresentado um design óptimo e confiável de uma roda de inércia usando um motor de corrente contínua sem escovas.

Apresenta-se ainda o design de todo o sistema, com destaque para o volante e com especial atenção à configuração e rearranjo de cada motor no sistema final. A massa do volante é minimizada tendo como restrições o momento de inércia necessário, a espessura e o tipo de material utilizado. O binário necessário e o binário ocasionado por perturbações externas também é analisado. A simulação dinâmica do SRI mostrou distúrbios sistémicos no binário aplicado, que se mostraram desprezáveis. Um modelo mais simples do motor utilizado é apresentado permitindo assim simular o SRI e como tal observar e avaliar a sua resposta. A determinação dos tempos médios de falha do sistema também foi considerada.

Finalmente, um protótipo totalmente funcional, que satisfaz todas as restrições e exigências é apresentado, bem como todos os testes realizados que demonstram a eficácia e a confiabilidade do SRI que irá ser integrado no micro-satélite ECOSat-III.

Palavras-chave: Sistema de Controlo; CubeSat; Roda de Inércia; Dinâmica e Controlo; Volante; Desenvolvimento e Design

Abstract

Stringent mission and payload designs in CubeSats, which are a type of miniaturized satellite for space research, require faster and more accurate pointing systems. These requirements can only be achieved by using reaction wheels for attitude control purposes. The thesis presents the design and development of a Reaction Wheel System (RWS) to be integrated on ECOSat-III mission, currently under development at the University of Victoria. The proposed design feature will enable a new classes of missions currently difficult to achieve.

The optimal design, reliability analysis, and construction of a miniaturized reaction wheel prototype using a commercial off-the-shelf brushless DC (BLDC) motor is presented.

The hardware design is described, with emphasis on the disk-rim flywheel design and on the RWS arrangement for minimum power consumption. Its mass is minimized subject to constraints on the required moment of inertia, flywheel thickness and type of material used. The required torque and the maximum external disturbance torque acting on the satellite are estimated. The dynamics simulation has shown negligible systemic torque disturbances. A simpler model of a BLDC motor is presented in order to model the RWS. The determination of the mean time to failure is also one of the objectives of the thesis.

Finally, a fully functional prototype, which satisfies all the constrains and requirements, is presented as well as all the tests performed to demonstrate the effectiveness and the reliability of the RWS to be integrated in the ECOSat-III micro-satellite.

Keywords: Control System; Cubesat; Reaction Wheel System; Flywheel; Dynamics and Control; Development and Design

Contents

List of Tables

List of Figures

Nomenclature

Greek symbols

α Nominal contact angle

α_ω^M Wheel angular acceleration relative to the body-fixed motor reference frame

β Dynamic frictional torque coefficient

β_1 Configuration angle relative to the x-axis

β_2 Skew or cant angle of each reaction wheel

δ_{play} Axial radial play in the motor axle

$\delta_{tolerance}$ Tolerance variation in the flat feature

Λ Ratio between the resultant oil film thickness and surface roughness

ω Angular velocity of the wheel

ω_0 Mean orbital angular velocity

ω_b Angular rate vector in the inertial body reference frame

ω_{rws} Angular rate vector of the Reaction Wheel System

ρ Material's density

ρ_{atm} Mean atmospheric density at the satellite orbital altitude

σ_a Tensile axial stress

σ_r Tensile radial stress

σ_θ Tensile tangential stress

θ_e Electrical angle of the rotor

θ_m Mechanical angle of the rotor

θ_{axle} Maximum motor shaft deflection

θ_{man} Deflection caused by manufacturing errors

υ Poison's ratio of the material

$f(\theta_e)$ Back-EMF reference function

Roman symbols

$\overline{R}_{rim}$ Mean radius of the rim

A Factor related with the viscosity of the lubricant

A_s Biggest surface area of the satellite

a_{ω}^{M} Wheel angular acceleration relative to the body-fixed motor reference frame

B Earth magnetic field

b Width of the rim

b_m Rating factor depending on normal material and manufacture quality

c Light speed

C_0 Motor static friction coefficient

c_a Aerodynamic center of the satellite

C_d Drag coefficient

c_g Center of gravity of the satellite

C_r Basic dynamic radial load rating

C_v Motor dynamic friction coefficient

c_{sp} Center of solar pressure of the satellite

D Residual dipole of the satellite

D_b Factor related with the bearing dimensions

D_w Nominal diameter of the ball bearing

$d_{bearing}$ Distance between the origin of the motor reference frame and the bearing exit

$E_a; E_b; E_c$ Back-EMF voltage of the motor for each phase

F_a Axial load on the bearing

F_c Total centrifugal force on the rim

f_c coefficient determined from shape, processing accurancy and material of bearing parts

F_r Radial load on the bearing

F_s Solar constant

h Angular momentum of the reaction wheel system

H_t Total angular momentum generated by the RWS

H_w Angular momentum vector of the wheel array

I Motor current

i Worst case incidence angle

I_0 Stall current of the motor

$i_a; i_b; i_c$ Motor input current for each phase

I_b Inertia tensor of the satellite

I_{rws} Inertia tensor of the Reaction Wheel System

I_w^M Inertia matrix of the flywheel w.r.t. the body-fixed motor reference frame

I_{yy} Moment of inertia of the satellite with respect to the Y-axis in the body reference frame

J Inertia moment of the motor coupled with the inertia moment of the wheel

k_e motor back-EMF constant

k_m Torque constant

k_w Back-EMF constant of one phase

L Armature self inductor

L_{10} Bearing life expectancy

M_{rim} Mass of the rim

n Rotational speed of the motor

P_r Dynamic equivalent radial load

P_{in} Input power

P_{out} Output power

P_{req} Power required

q Reflectance factor

R Factor related with the rotational speed

r Inner radius of the rim

$R^{\omega t}$ Time-dependent transformation matrix

$R^{M/R}$ Transformation matrix that transforms a vector expressed in the rotor reference frame in the motor reference frame

R_i Inner radius of the rim

R_o Vector that expresses the distance from satellite to the mass center of the attracting body

r_o^M vector from the body-fixed motor reference frame origin to the origin of the rotor reference frame

R_t Terminal resistance, phase-phase

r_w^M Vector from the origin of the body-fixed motor reference frame to the flywheel center of mass

r_w^r vector from the origin of the body-fixed motor reference frame to the flywheel center of mass expressed in the rotor reference frame

R_{out} Outer radius of the rim

r_{wheel} Disk-rim flywheel radius

T DC motor resulting torque

t Disk thickness

T^{fw} Disturbance torque vector

$T_a; T_b; T_c$ Electromagnetic torque generated by each phase

T_e Electromagnetic torque of the motor

T_g Torque caused by the gravity gradient

T_r Resistance torque

T_t Total torque generated by the RWS

T_w Torque vector of the wheel array

T_{aero} Torque caused by the aerodynamic forces

T_m Torque caused by the magnetic field

T_{req} Torque required

$T_{s_{y+}}$ Torque required around the $y+$ axis of the inertially body frame to performed the desired manoeuvre above victoria

T_{sr} Torque caused by the solar radiation

U Voltage applied to the motor

V Linear orbital velocity relatively to Earth inertial reference frame

$V_a; V_b; V_c$ Terminal phase voltage of the motor

W Distribution matrix that transform the wheel frame to the body frame

x_{cgeo} X coordinate of the center of mass of the satellite relative to its geometric center

y_{cgeo} Y coordinate of the center of mass of the satellite relative to its geometric center

Z Number of rolling elements per row

z_{cgeo} Z coordinate of the center of mass of the satellite relative to its geometric center

Glossary

AC	Alternate Current
ADCS	Attitude Determination and Control System
BLDC	Brushless Direct Current
COTS	Commercial off-the-self
CSDC	Canadian Satellite Design Challenge
CS	Control System
ECOSat	Enhanced Communications Satellite
EHD	Elasto Hydro Dynamic
EMF	Electromotive force
ESTL	European Space Tribology Laboratory
GSFC	Goddard Space Flight Center
MOSFET	Metal–Oxide–Semiconductor Field-Effect Transistor
MTTF	Mean Time To Failure
NASA	National Aeronautics and Space Administration
NITK	National Institute of Technology Karnataka
RWS	Reaction Wheel System

Chapter 1

Introduction

The use of satellites for scientific, commercial and military purposes has been rising year after year. Over the past years there has been a huge investment in miniaturizing the space technology and this has given origin to a new kind of satellites - the nanosatellites. These satellites are in a range between 1 kg to 10 kg and have become an increasingly popular alternative over the traditional more bulky satellites [1]. One reason for miniaturing satellites is to reduce the cost, i.e., heavier satellites require larger rockets with greater thrust. On the other hand, smaller and lighter satellites require small and cheaper launch vehicles, as well as they can be integrated in multiple launch projects or on the excess capacity of larger launch vehicles.

The decreasing cost of this miniaturized satellites are making them accessible to academia and student-led projects. Within this group of satellites, there is a specific class of satellites, which have a volume of exactly one liter and a mass of no more than 1.33 Kg - **the CubeSats** [2]. The first CubeSat designed was proposed in 1999 by Professors Bob Twinggs and Jordi Puig-Suari, and the main goals was to provide an opportunity for graduate students to design, build, test and operate a smaller spacecraft [3].

1.1 General context

1.1.1 The ECoSat project

In September 2010, Geocentrix (a Canadian company) organized the first Canadian Satellite Design Challenge (CSDC) and invited twelve universities across Canada to design and develop a micro-satellite [4]. This challenge has contributed to an increase in expertise and training of highly-qualified personnel at several universities during the development of a $3U$ CubeSat.

To participate in this competition, the University of Victoria proposed the development of a micro-satellite, the Enhanced Comunications Satellite (ECOSat), and developed by a multidisciplinary group of students and faculty mentors. Simultaneously, one of the objectives of this group is also get involved in the community by actively working with small schools, different organizations and international outreach [5]. The know-how acquired from the fully in-house designed CubeSat with power, command and data handling, mechanical, and payload systems has been an invaluable tool in training of future space engineers and UVic attained a 3^{rd} place during the phase one of the program in 2012 [6]. In 2014, during the 2^{nd} phase of the CSDC program, ECOSat placed 1^{st} in the competition and won the prize and right to launch the CubeSat into orbit. This gave origin to the 3^{rd} phase of the project: the ECOSat-III project.

ECOSat-III will be flying a primary hyperspectral imaging payload, supported by an experimental communications system and attitude control system. Thus, there are several assignments to accomplish in the next phase of the competition [7],

- Provide hyperspectral imagery of Canada at 150-meter resolution.
- Downlink the hyperspectral imagery over a custom-developed 40 MBit communications system.
- Improve ECOSat-III Attitude Determination and Control systems with the addition of momentum wheels and more complex attitude determination algorithms
- Provide accurate initial orbit determination and low rate telemetry through the use of an experimental below-the-noise-floor communications system.

1.1.2 Thesis Motivation

The mission of these CubeSats require precision pointing, and therefore there is a need for an Attitude Determination and Control System (ADCS). On the previous generation satellite, ECOSat-II, this subsystem used GPS and magnetic map data for attitude determination and magnetorquers as a Control System (CS) [8]. Now, that the ECOSat group has moved into the third round of the CSDC a new design for the ADCS must be implemented. Magnetorquers have a full range of control at polar orbits, and become less effective at lower inclination orbits. The ECOSat-III mission will have an orbital inclination of $i = 51.6°$. Moreover, due to the primary mission requirements, a precise pointing is required which cannot be achieved if the satellite only uses magnetorquers. Thus, the ADCS must consist also of multiple reaction wheels that spin at fast enough rates to allow the conservation of angular momentum in order to generate control torques on the rotation axis, so that the satellite can turn about this fixed axis and orient itself in the desired direction.

There are several companies working on the miniaturization of Reaction Wheel Systems (RWS), to be integrated on the ADCS of micro-satellites. These actuators can be very expensive (in the order of 10^4 to 10^5 dollars) [9]. The performance of the RWS is quantified by the maximum angular momentum, maximum output torque, electrical power, and the level of micro-vibrations produced by the wheels. Current research focuses on increasing angular momentum and maximum output torque, and decreasing electrical power and micro-vibrations [10]. There are several reaction wheels available on the market which could be considered and used on ECOSat-III. However, the use of these off-the-shelf solutions would have a high cost for the project. Another factor that was taken into consideration relates the durability of the system. Currently, RWS designed for CubeSats are not able to operate in harsh space conditions for more than 1 year. Moreover, creating a RWS in-house enables a better learning, understanding and know-how for future missions.

According to a NASA report on the state of the art in small spacecraft technology [10] the world smallest proven reaction wheel, RW1, was used on BEESAT, a picosat design and operated by TU Berlin, and it had a mass of approximately 72 g [11]. However the estimated mean time to failure (MTTF) is approximately one year which is not compatible with the mission objectives for ECOSat-III that requires a MTTF of 2 years.

In this thesis, the design and implementation of a in-house developed RWS is proposed and, after manufacturing and validation, will become an important component of a space qualified ECOSat-III.

1.1.3 Methodology

Consistent project methodology provides structure for high quality deliverables. In the case of the development of the RWS it is fundamental to determine the needs and the goals of this project. Throughout this thesis there is a specific methodology that was followed, and the main objective is to demonstrate that is feasible to construct a reliable and inexpensive RWS which fulfils all the missions requirements. Thus, the following methodology, presented in Fig. 1.1, is proposed and should be considered hereinafter.

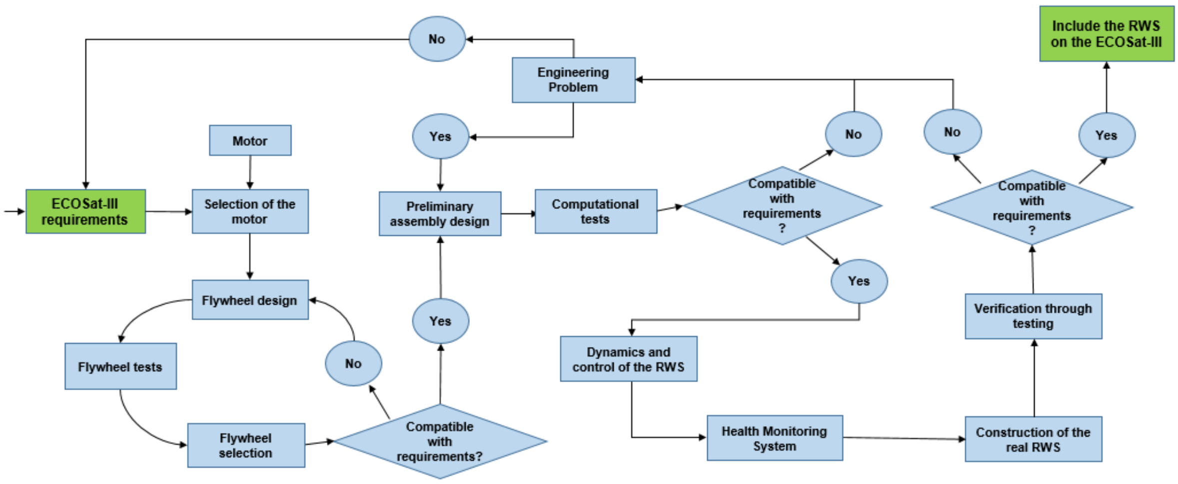

Figure 1.1: Proposed methodology to be used in the design and construction of the RWS

It was agreed that the use of a commercial-of-the-shelf (COTS) motor should be considered, due to time constrains and specially due to its reduced dimensions it would be more expensive to construct an in-house motor. After the selection of the desired motor, the design of the flywheel must be considered, based not only on specific requirements, but also on several constrains that must be fulfilled. If the optimum design is in accordance with ECOSat requirements then a preliminary assembly design must be proposed and simulated in order to determine if there are any internal perturbation torques that can influence the RWS adversely. Following this analysis, a dynamic model of the all system must be simulated and consequently integrated on the Attitude Determination and Control System (ADCS) simulation of the complete satellite system. Simultaneously, an estimation of the MTTF and a reliability analysis of the system shall be made. A specific control system for the selected motor should also be studied as well the implementation of some concepts to perform health monitoring for the RWS. Several tests should be also performed in order to validate the selected motor for space applications. This will finally end up in the construction of the RWS prototype to be incorporated on the ECOSat-III. Due to time constrains, the construction and final analysis of the complete and integrated system, and the implementation of health monitoring methods in the RWS will not be considered in this thesis.

1.2 Theoretical Background

The main objective to be achieved is to design and construct a reliable RWS to be integrated on ECOSat-III. This RWS must take into consideration the following constraints: the maximum allowed mass, volume, durability and reliability of the all systems.

1.2.1 Basic concepts and equations

The governing equations for the satellite's attitude are expressed using angular kinetic and angular kinematics equations. Angular kinetic equations express the rate of change in angular velocities due to external torques and disturbances. The angular kinematics equations specify the relationship between absolute angular velocity of the satellite and its orientation in the space [12].

According to the angular kinetic equations an object that is spinning has a rotation associated with it, known as its angular momentum. The total angular momentum, L, of the satellite can de written as [13],

$$L = I_s \omega_b + h \tag{1.1}$$

where $h = I_{rws}\omega_{rws}$ is the angular momentum of the RWS, I_s is the inertia tensor of the satellite and ω_b is the angular rate vector in the satellite's fixed-body reference frame.

The time derivative of L, in relation to the inertially fixed coordinate system, $\frac{dL}{dt}\big|_I$, can be written as:

$$\left.\frac{dL}{dt}\right|_I = \left.\frac{dL}{dt}\right|_B + \omega_b \times L \tag{1.2}$$

where $\frac{dL}{dt}\big|_B$ is the time derivative of the angular momentum relatively to the satellite's fixed-body reference frame. If the external torques are neglected, the total angular momentum is conserved, i.e. $\frac{dL}{dt}\big|_I = 0$. However, in real orbital conditions $\frac{dL}{dt}\big|_I \neq 0$, which is caused by forces that act on the satellite such as the solar radiation, gravity gradient, magnetic field and aerodynamics. Furthermore, it is also assumed that the moments and products of inertia of complete system remain constant. Thus, it is possible to infer that:

$$I_s \dot{\omega}_b + \dot{h} + \omega_b \times (I_s \omega_b + h) = \left.\frac{dL}{dt}\right|_I \tag{1.3}$$

As an initial simplification, it will be assumed that the direction of the vector that expresses the total angular momentum of the satellite, L is coincident with the direction of the angular rate vector of the satellite w.r.t the body reference frame, meaning that $\omega_b \times (I_s\omega_b + h) = 0$. In summary, as a consequence of the law of conservation of the angular momentum, it is possible to define an active system able to control the angular rate of the satellite during its orbital movement. This will allow the design and manufacturing of a RWS able to control the attitude of the satellite.

1.2.2 Requirements and constrains

ECOSat-III has several requirements and constrains, which shall be considered before starting developing an operational RWS. They have evolved significantly over the course of the project. This evolution will not be described here, but only the final requirements and constraints.

Requirements	Description
[Eco/ADCS-170]	The ADCS shall consume less than 1W during nominal operations.
[Eco/ADCS-190]	ECOSat must be able to rotate at 1 revolution per orbit.
[Eco/ADCS-200]	The entire ADCS system must weigh less than 250 g.
[Eco/ADCS-320]	The ADCS must survive fluctuating temperatures of -40 to $+125$ degrees Celsius.
[Eco/ADCS-330]	The ADCS must be able to operate in a fluctuating temperature range of -30 to $+85$ degrees Celsius.

Table 1.1: Main requirements to be used on the RWS design

In the preliminary design of the ECOSat-III, a structural analysis was performed by neglecting the effect of some sub-systems of the satellite, including the RWS [7]. This analysis has provided data such as an estimate for the satellite's center of mass ,$(x_{cgeo}, y_{cgeo}, z_{cgeo})$, relative to the geometric center of the satellite, its inertia tensor I_b and total mass, m_s.

Properties	Value
m_s	3.66 kg
$(x_{cgeo}, y_{cgeo}, z_{cgeo})$	$(2.6589, -0.0082, 0.3078)$ mm
$I_b = \begin{bmatrix} I_{xx} & I_{xy} & I_{xz} \\ I_{yx} & I_{yy} & I_{yz} \\ I_{zx} & I_{zy} & I_{zz} \end{bmatrix}$	$\begin{bmatrix} 6.885 \times 10^{-3} & 1.998 \times 10^{-5} & -5.199 \times 10^{-5} \\ 1.998 \times 10^{-5} & 3.517 \times 10^{-2} & 0.499 \times 10^{-5} \\ -5.199 \times 10^{-5} & 0.499 \times 10^{-5} & 3.617 \times 10^{-2} \end{bmatrix}$ kg.m^2

Table 1.2: Spacecraft characteristics summary [7]

Is is also important to define the orientation of the fixed-body reference frame of the satellite. It will be assumed that the fixed-body reference frame of the satellite will be oriented in relation to the nadir point (+Z-axis) and the velocity vector (+X-axis), as seen in Fig. 1.2

After defining the requirements, the characteristics of the satellite and the orientation of the body axes, it is important to define the required torque that shall be provided by the RWS in order to perform the required manoeuvres for this mission.

ECOSat-III will have a circular orbit around 800 km above Earth's surface. Moreover, one of the main

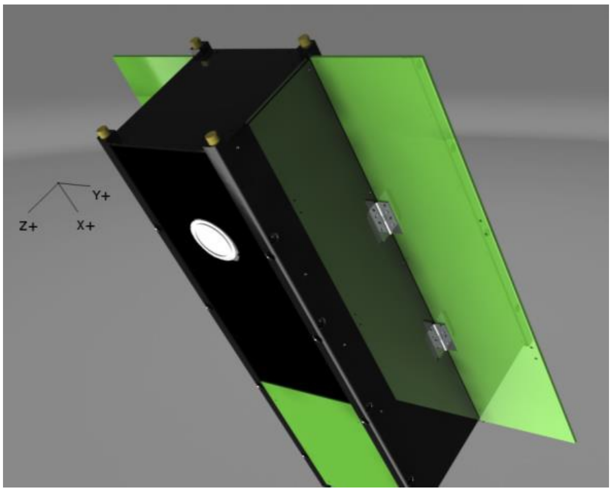

Figure 1.2: Body axis orientation of ECOSat-III [7]

objectives of this CubeSat's mission is to provide hyperspectral imagery of Canada at 150-meter resolution. Another objective refers to the mission ground track and to the ground station access. According to the ECOSat team [7] simulations for the orbit of the satellite, using STK - AGI software, the angular rate of the satellite above Victoria around the Y-axis of the satellite w.r.t. the fixed-body reference frame is presented in Fig. 1.3.

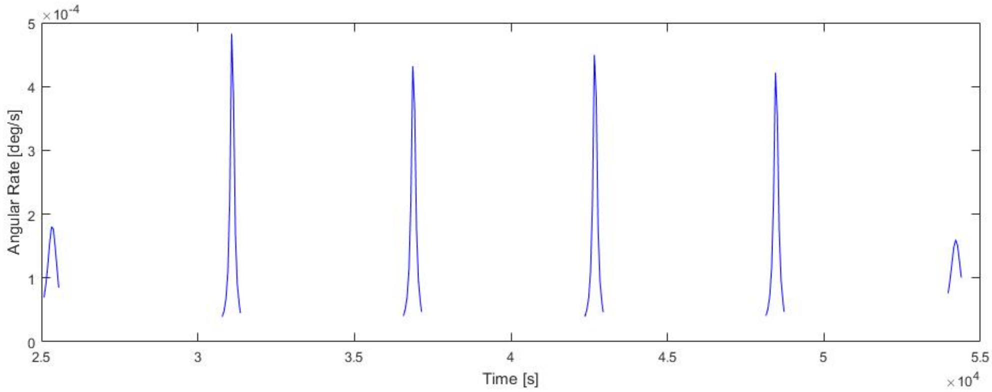

Figure 1.3: Angular rate [deg/s] of ECOSat-III above Victoria

Here, each peak corresponds to the angular rate of one crossing of the satellite above the UVIC's Ground Control Station in a total of six crossings during one day. The obtained data assumes that no external disturbances act on the satellite. Moreover, implementing this manoeuvre will enable the hyperspectral camera to be pointing during the maximum duration to a specific point on Earth, in this case into the direction of the ground track facility in Victoria, BC, since its ascension on the horizon.

Then the torque, required to rotate the satellite with such angular rate can be easily determined by simple deriving the data obtained by STK (see Fig. 1.3) and by making use of the following relation,

$$\begin{bmatrix} T_{s_{x+}} \\ T_{s_{y+}} \\ T_{s_{z+}} \end{bmatrix} = I_b \begin{bmatrix} 0 \\ \ddot{\theta} \\ 0 \end{bmatrix} \tag{1.4}$$

where $[T_{s_{x+}}, T_{s_{y+}}, T_{z_{x+}}]^T$ is the torque vector that shall be delivered by the satellite w.r.t. the fixed-body reference frame considering the absence of external perturbations, and $\ddot{\theta}$ is the angular acceleration of the satellite around the Y-axis in the body reference frame.

Thus, it is now possible to determine the torque that needs to be delivered around the Y-axis of the satellite w.r.t. the body reference frame,$T_{s_{y+}}$, in order to perform the desired manoeuvre, see Fig. 1.4.

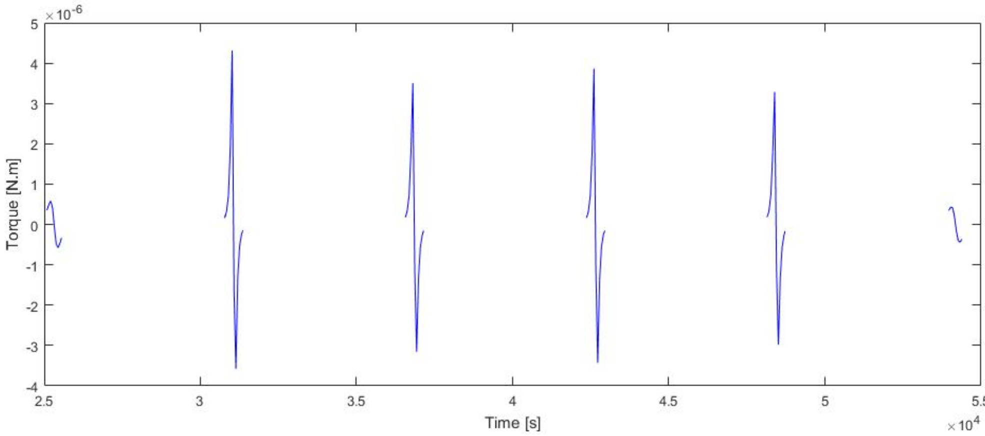

Figure 1.4: Torque that should be applied on ECOSat-III during its crossing above Victoria (maximum angular rate), considering the absence of external perturbation torques

This assumes there are no disturbance forces acting on the satellite. However, in real space conditions, this assumption is not truly correct and several forces will exert external perturbation torques to the satellite. In 1.3 this external forces will be analysed in order to get more precise and accurate results about the actual torque that shall be applied to each axis of ECOSat-III.

1.3 External perturbation torques

Even in space, there are natural forces that in turn make bodies tumble. These forces are caused by solar radiation, gravity gradient, Earth magnetic field and aerodynamics. In the context of attitude and control this forces are called disturbance forces.

1.3.1 Gravity gradient

Gravity gradient torques result from the fact that two opposing points of the spacecraft have a finite distance in a declining potential field [14, 15].

$$T_g = \frac{3k}{R_o^3}(R_e \times I_b \cdot R) \tag{1.5}$$

where $k = \omega_0^2 R_e^3$; ω_0 is the mean orbital angular velocity in [rad/s]; R_e is the vector that expresses the distance from satellite to the mass center of the Earth.

1.3.2 Solar radiation

The radiation emitted by the Sun generates a pressure on the satellite's surface. This pressure generates a torque, which can be modulated accordingly to the following formula, [14, 16]

$$T_s = \frac{F_s}{c} A_s(1+q)cos(i)(c_{sp} - c_g) \tag{1.6}$$

Since the upper bound is the only interesting solution, the worst case incidence angle occurs when $i = 0°$. F_s is the solar constant, which for a satellite at 800 km altitude is $F_s = 1367$ W/m^2 [16]. $A_s = 0.10 \times 0.30$ cm^2, which is the surface area of biggest incident of direct solar radiation. It will be assumed the worst case, where the center of mass,c_g, is located in the center of the satellite and the center of solar pressure,c_{sp}, acts in the furthest possible area of the longest face, ı.e. $c_{sp} - c_g = 0.15$ cm. According to J.Wertz [14] the typical reflectance factor is $q = 0.6$.

1.3.3 Earth magnetic field

The spacecraft's motion across the geomagnetic field induces an electromagnetic field in the spacecraft which in return interacts with the geomagnetic field. This generates a disturbance torque [14, 17],

$$T_m = BD_{res} \tag{1.7}$$

where B is the Earth's magnetic field in Tesla. For polar orbits the Earth's magnetic field is $B = 2M/R_e^3$, where $M = 7.96 \times 10^{15}$ T m^3 (magnetic momentum) and for equatorial ones is half of that value. Thus, an arithmetic weighting between both values is considered, based on the fact that the orbital inclination of the satellite is $i = 51.6°$. Since there are no data yet available about the antenna and the magnetorquer that are going to be integrated on ECOSat-III, the residual dipole (D_{res}) must be estimated based on previous available data on CubeSats.

Based on Korean Hausat-1 and on the Danish AAUSat [17] the values for magnetic activated control satellites(magnetorquers) are between 0.022 A.m^2 and 0.075 A.m^2, respectively. Thus, for ECOSat-III a good initial estimative would be $D_{res} = 0.048$ A.m^2, which corresponds to the arithmetic mean of these values.

1.3.4 Aerodynamics

Forces caused by aerodynamics should also be considered, specially for low Earth orbit satellites, since the atmospheric pressure can not be entirely negligible. This force can be used in order to estimate the maximum aerodynamic torque acting on the satellite [18]. Thus, the following relation is derived:

$$T_{aero} = \frac{1}{2}(\rho C_d A V^2)(c_a - c_g) \tag{1.8}$$

where $\rho = 9.59 \times 10^{-13}$ kg/m^3, considering the average density between the solar maximum and the solar minimum [19]; $A_s = 0.10 \times 0.30$ cm^2 is the biggest surface area; V is the satellite orbital velocity relative to Earth inertial reference frame; c_a the aerodynamic center and c_g the center of gravity. For the same reason used for the solar radiation perturbation torque, it will be assumed that $c_a - c_g = 0.15$ cm. The drag coefficient was assumed to be $C_d = 2.5$ [18, 20].

1.3.5 Total maximum magnitude

In space, each external perturbation torque has a specific torque vector associated with it. Nevertheless, for the preliminary design, the only required factor to be considered is the upper bound of these perturbation torques, i.e. the worst case torques. Then, it will be assumed that all the external perturbation torques are acting in the same direction simultaneously at the maximum possible magnitude. The magnitude of the torque determined will be replied to each axis of the body reference frame. This assumption was used due to the lack of data for the preliminary design. Nevertheless, it represents a good estimate for the real perturbation torques magnitude that the satellite will be subject to. These external perturbation torques are expressed in Table 1.3

Perturbation torque	Magnitude [Nm]
Gravity gradient	4.3×10^{-8}
Aerodynamic	2.9×10^{-7}
Solar radiation	8.2×10^{-9}
Magnetic field	2.0×10^{-6}
Total	2.4×10^{-6}

Table 1.3: Magnitude of each principal external perturbation torque

Chapter 2

Reaction Wheel System Design

As mentioned in Chapter 1 it was early decided in the development of the RWS of ECOSat-III that the RWS should be designed in-house on the basis of a commercial off-the-shelf motor. In this Chapter a summary of the system engineering activities that were responsible for the development of the ECOSat-III RWS are going to be presented.

Firstly, the available solutions are going to be described. Particular only Brushless Direct Current (BLDC) motors are going to be considered. Also, a briefly introduction to the arguments behind this choice followed by a summary of the selection criteria and the final trade-off for the motor that is going to be used in the RWS is presented. After the design of the flywheel is characterized, considering the minimization of the mass, as well as the radial stresses induced by its rotation, in order to select the best design to be implemented in ECOSat-III RWS. Finally, an analysis to the RWS configuration is going to be presented in order to determine the optimal arrangement of each wheel, taking into account redundancy factors and also the minimization of the power consumption.

2.1 Available solutions

In space applications, it is highly desirable to eliminate all types of surface contacts, bearings and gear drives, as well as electrical brushes. In support to future space missions, Goddard Space Flight Center (GSFC) established a program, which had the objective to manufacture a new type of motor highly desirable for space applications. Under contract to the National Aeronautics and Space Administration, NASA, Sperry-Garragut developed the first in a series of BLDC motors that would see use in many parts of the Space Program [21].

The principle of photoelectric sensing of rotor position and electronic commutation of the motor was proved feasible [21]. These DC motors were the first to demonstrate self-starting capability. In addition they have higher efficiencies when compared to the Alternative Current, AC, motors, and they are qualified for long-term space missions. Moreover, the operability time is bigger when compared to brushed motors. This came from the fact that BLDC motors do not have brushes, meaning the operating life time is mainly limited by bearing failure [21, 22], which will be further analysed in Chapter 5.

With the development of miniature Hall sensors, the basis for the modern-day BLDC motors was completed. BLDC motors are believed to be the optimal choice for reaction wheels thanks to their linear, symmetric torque response, efficiency and durability. This linearity breaks down at the rotation speed zero-crossing, where the motor demonstrates highly non-linear behaviour due to the static friction that needs to be overcome to accelerate the BLDC from zero rotation speed [23]. This friction is mainly caused by bearing friction [21].

Thus, it shall be very useful to operate the motor out of the zone of non-linearity, as well as to avoid the zero-crossings. The reason why this operational limits should be applied to the motor will be explained and better understood along this dissertation.

2.1.1 Selection Criteria

For the selection of the BLDC motor that is going to be mounted in ECOSat-III RWS there are several requirements that should be fulfilled. Some of them were already described for the all the RWS, while others were created in order to fulfil the mission objectives;

- The motor should be able to operate in a fluctuating temperature range of -30 to $+85$ degrees Celsius, which is the temperature variation the satellite will suffer during its operation in the low Earth orbit;
- The selected motor should be vacuum proof. A non-vacuum lubricant implies an heavier, hermetically closed, cage and consequently an increase in the cost of the satellite. Moreover, its operability would be corrupted if the RWS lost its pressure, for instance due to micro perforations caused by meteorites.
- The maximum torque provided by the motor should be bigger than the sum of the disturbing torque with the torque required to perform all the manoeuvres above Victoria, B.C;
- Its volume and dimensions should not compromise the useful volume needed in order to integrate all the other components on ECOSat-III;
- The existence or not of sensors to determine the rotational speed; The most common integrated sensor available for this motor are hall sensors, which gives the rotational speed of the rotor;
- The cost of the motor and all extra external components. BLDC motors are more expensive to manufacture than brushed DC motor and they also require an additional cost due to external components, specially required to control the commutation sequence.

2.1.2 Selected motor

Hereupon, there are several parameters that should be considered in the selection of the adequate, commercial off-the-shelf (COTS) BLDC motor. For that, it was necessary to make an comprehensive market research of high quality motor manufactures for candidates that shall deliver the required torque and simultaneously fulfil all the aforementioned criteria factors.

Model/Requirements	1202 004 BH (FH)	1608 004 BH (FH)	2209T005S (FH)	EC 10 flat (MX)	EC 6 flat (MX)
Torque [mNm]	0.16	0.205	0.094	0.24	0.339
Temperature range [ºC]	-30 to $+85$	-30 to $+85$	-30 to $+85$	-40 to $+85$	-20 to $+100$
Maximum Velocity [rpm]	40000	12000	10000	15000	25500
Nominal Voltage [V]	4	3	5	4	6
Power [W]	0.652	0.116	0.06	0.2	1.5
Sensor	Hall Sensor	Hall Sensor	Hall Sensor	Hall Sensor	Hall Sensor
Cost [$]	82.77	121.45	177	170	140

Table 2.1: Comparative analysis of several available motors presently available at the market

All motors presented in Table 2.1. have the advantage of having incorporated hall sensors, which will aid and simplify the controllability of the motor. Simultaneously, it also avoids the need of extra peripheral components to determine the rotational speed of the motor. The maximum rotational speed is also another factor to consider during the motor selection, since the bigger the nominal rotational speed during a specific manoeuvre, without being in the saturation domain, the smaller will be the flywheel. As result, lighter will be the system. Almost all the aforethought motors are able to operate, theoretically, inside the fluctuating temperature range. The cost of the motor is also one of the main factors to consider, since one of the objectives of this thesis is to prove that is possible to construct a reliable and low-cost RWS.

Thus, based on the maximum useful speed and on the temperature range, it is possible to conclude that FAULHABER 1202 004BH (see Fig. 2.1) is the best motor to be used in ECOSat-III, as part of the RWS. A negative factor to consider relates to the fact that any of the investigated motors are designed for vacuum conditions. However, it is possible, according to the FAULHABER Company to replaced the original lubricant by an ultra high vacuum lubricant. All the characteristics of the selected motor can be consulted in Appendix A

Figure 2.1: FAULHABER 1202 004 BH [24]

2.1.3 Maximum useful speed

From the requirements and also from the STK simulation already presented in Chapter 1, the maximum torque expected to be delivered by the RWS to the Y-axis of the satellite w.r.t. the body reference frame in order to guaranty the desired manoeuvre should be 6.83×10^{-6} N.m. As an initial simplification to determine the maximum useful speed of the motor, some assumptions are going to be made:

- There is no data yet available for the configuration of the wheels, so it will be assumed the worst case, i.e. each wheel will be aligned with the axis of the satellite in the body reference frame, meaning that the maximum torque provided by the wheel that is aligned with the Y+ axis of the satellite should be 6.83×10^{-6} N.m (sum of the torque provided by the manoeuvre and the one from the external perturbations);

- As a matter of simplification in order to determine the maximum useful speed the BLDC motor is going to be analysed assuming a simplified DC motor model.

This will be defined for the selected motor which is the maximum useful speed at which the flywheel shall rotate.

In a DC motor the following relations are well understood [23]:

$$k_m I = T + T_r = T + k_m I_0 \tag{2.1}$$

where, T [N.m] is the resulting torque, T_r [N.m] is the resistance torque, k_m is the torque constant and I_0 [A] is the stall current of the motor.

The current intensity in the motor, I [A], as well the stall current, I_0, can be expressed as,

$$I = \frac{U - k_e n}{R}, \tag{2.2a}$$

$$I_0 = \frac{C_0 + C_v n}{k_m}, \tag{2.2b}$$

where, C_0 is the motor static friction coefficient; C_v is the motor dynamic friction coefficient; R is the motor resistance, phase-phase [Ω]; k_e the motor back-EMF constant and n is the motor rotational speed [rpm]. By rearranging equation 2.3 it can be concluded that,

$$T = \Big(\frac{U - k_e n}{R} - \frac{C_0 + C_v n}{k_m}\Big) k_m. \tag{2.3}$$

Based on the aforementioned relation the characteristics for the power consumption of the motor can be determined. It is known that the input power, P_{in} $[W]$ delivered by the battery or the electrical source of energy and the output power, P_{out} $[W]$ delivered by the axial shaft of the motor can be determined using the following relations,

$$P_{in} = UI = U\Big(\frac{U - k_e n}{R}\Big), \tag{2.4}$$

$$P_{out} = \frac{2\pi n}{60} T. \tag{2.5}$$

Nevertheless, to obtained the torque already specified, $T_{req} = 6.83 \times 10^{-6}$ N.m, the required input power is given by,

$$P_{req} = U\big(I_0 + \frac{T_{req}}{k_m}\big) \tag{2.6}$$

Thus, the power input shall be bigger than the power required for a specific torque at a determined speed assuming a nominal voltage of $U = 4$ V. Therefore, Fig. 2.2 can be obtained,

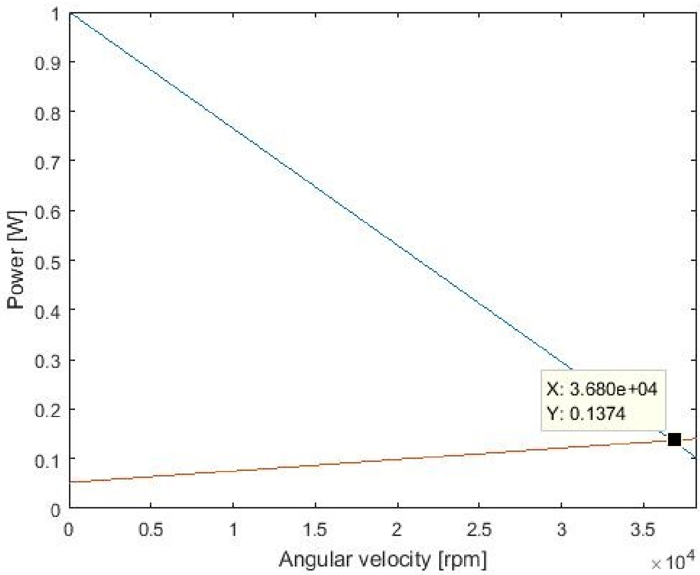

Figure 2.2: Maximum useful speed the motor can delivered for T_{req}. The blue line corresponds to the P_{req} and the red line corresponds to the P_{in} for and input voltage of $U = 4$ V

In conclusion, it was easy to determine that the maximum useful speed is $\mathbf{36800\ rpm}$. Hereupon, it will be assumed the operational rotational speed equals to half of the maximum useful speed $\mathbf{18400 rpm}$. This means the voltage delivered by the battery for each motor in order to have this rotational speed shall be $U = 2.1$ V.

2.2 Flywheel Design

The value of the maximum speed n_{max} is of primary importance in the flywheel's design, since higher speeds results on a higher momentum storage, but simultaneously on an higher centrifugal stresses which should not exceed the admissible values of the selected material.

As modern designs require light weight, the design parameters are chosen in order to ensure minimum mass and additionally minimum stresses. Both of this requirements are essential for the design of the flywheel that is going to be integrated on ECOSat-III RWS. Lighter mass of the satellite implies a reduce in its launch costs. Moreover, the stresses at which the flywheel will be subject will also determine the durability of the RWS, which as it will be analysed in this thesis will have a negligible impact on it. Nevertheless, the present method here developed can be applied to the design of a flywheel with other industrial or technological applications.

2.2.1 Design criteria

The moment of inertia of a mass element about a given axis is proportional to the square distance between the element and its axis. Thus, smaller mass at a large distance is more preferable than a larger mass at small distances, from the point of view of the minimum weight. However, in bodies of revolution, larger distances imply larger circumference and areas [25]. To ensure this, a rim-disk flywheel is suggested [26].

In sum, these factors must be investigated properly in order to achieve the optimum design for the flywheel mass considering at the same time the radial stresses at which the wheel is going to be exposed.

Different aspects of flywheel designs were investigated by several authors along with other rotating disk machine elements. You et. al. [27] made numerical analysis of elastic plastic rotating disks with arbitrary variable thickness and density; the governing equation is derived from the basic equations of rotating disks. Nevertheless, a much more simple model will be used in this thesis, since it is going to be considered a disk-rim flywheel with uniform density and thickness. Bedier and Naggar [28] developed a method to minimized the mass of the flywheel subject to constrains of required moment of inertia and admissible stress; the major theoretical assumptions are based on the theory of the rotating disks of uniform thickness and density which were applied independently to the disk and the rim with a suitable matching condition at the junction.

2.2.2 Simplified analytical model

As an initial starting point a disk-rim flywheel (see Fig. 2.3) is going to be considered. It should be indicated that the flywheel is fitted with a hub around the axis of rotation for mounting around the shaft. This hub serves as a reinforcement of the disc and neglecting it in the calculation will be an approximation in the safe side [28].

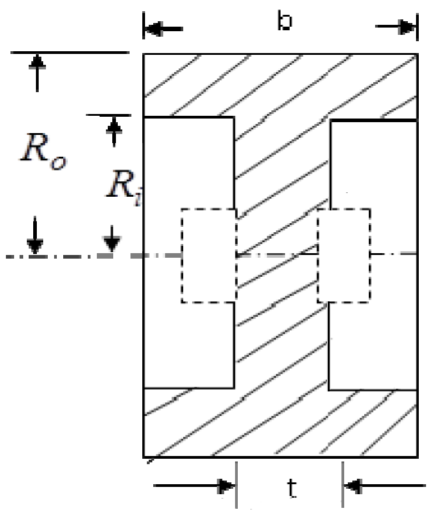

Figure 2.3: Disk-rim flywheel scheme [28]

The aforementioned disk-rim flywheel is going to be defined according to several parameters, namely R_0, which is the outer radius of the rim; R_i, which is the inner radius of the rim; b associate to the width of the rim and t that corresponds to the disk thickness.

This disk-rim flywheel is subject to internal stresses due to the inertial forces as result of its rotational speed. Under the action of the inertial forces only the three principal stress will be considered: σ_r, tensile radial stress; σ_t tensile tangential stress and σ_a, axial stress, which is generally also a tensile. The stress conditions occur throughout the section and vary primarily relative to the radius r. It is assumed that the axial stress σ_a is constant along the length of the section and because the disk is thin when compared to its diameter. Thus, axial stress throughout the section is assumed to be zero, $\sigma_a = 0$. Moreover, the internal and the external pressure are also going to be consider as zero. Thus, according to Bedier and Naggar [28],

$$\sigma_r = \frac{A}{2} - \frac{3-\upsilon}{8}\rho\omega^2 r^2 + \frac{B}{r^2} \tag{2.7}$$

$$\sigma_\theta = \frac{A}{2} - \frac{1+3\upsilon}{8}\rho\omega^2 r^2 + \frac{B}{r^2} \tag{2.8}$$

where υ is the Poison's ratio of the material; ω is the angular velocity of the flywheel; ρ is the material density and A and B are arbitrary constants to be determined from the boundary conditions imposed on both the disk and the rim.

From the previous equations 2.7 and 2.8 it can be easily concluded that $B = 0$, since $B/r^2 = 0$ gives the only finite solution for the resolution of this problem. The maximum value for the radial and the tangential stress occurs at the center of the disk, where $r = 0$.

Nevertheless, there is still yet to determine the arbitrary constant $A/2$ from the boundary condition at $r = R_i$, where the disk and the hub join together. This condition is imposed by the centrifugal force on the rim transmitted to the edge of the disk as radial stress ($\sigma_r|R_i$).

The total centrifugal force on the rim can be computed assuming all the rim mass, M_{rim}, is concentrated along the mean radius of the rim, $\overline{R}_{rim} = \frac{1}{2}(R_i + R_0)$. Moreover, the mass of the rim is considered to be uniformly distributed, which implies that $M_{rim} = \rho\pi b(R_0^2 - R_i^2)$. Hereupon, the centrifugal force,F_c, is given by,

$$F_c = M_{rim}\omega^2\overline{R}_{rim}. \tag{2.9}$$

It must be also assumed, that the area over which this force is uniformly distributed is the contact area between the disk and the rim, given by $2\pi R_i t$. Thus, the resulting radial stress at the disk edge is given by:

$$\sigma_{r|R_i} = \frac{1}{4}\rho\omega^2 R_i^2 y(x^2-1)(x+1) \tag{2.10}$$

where $y = b/t$ and $x = R_0/Ri$. By using the previous Eq. 2.10 as a boundary condition, the solution for the value of the constant A in Eq. 2.7 and Eq. 2.8 can be easily calculated.

Since the maximum radial stress occurs at $r = 0$, it is easy to conclude that

$$\sigma_{r_{diskmax}} = \sigma_{\theta_{diskmax}} = \frac{A}{2} = \rho\omega^2 R_i^2 \left[\frac{3+\upsilon}{8} + \frac{1}{4}y(x^2-1)(x+1)\right]. \tag{2.11}$$

Based on the aforementioned relations it is now possible to define the two objective functions that shall be used in in order to optimize the mass, Eq. 2.12, and the maximum radial stress, Eq. 2.13 for different flywheel configurations,

$$M_{disk-rim}(R_i, y, x) = \rho\pi R_i^2 t[1 + y(x^2-1)], \tag{2.12}$$

$$\sigma_{r_{diskmax}}(R_i, y, x) = \rho\omega^2 R_i^2 \left[\frac{3+\upsilon}{8} + \frac{1}{4}y(x^2-1)(x+1)\right]. \tag{2.13}$$

2.2.3 Shape optimization

After defining the simplified analytical model, a shape optimization for the geometric parameters of the disk-rim flywheel was considered.

The major objective to optimize is the mass of the flywheel. Another factor to take into account is the radial and the tangential stresses at which the flywheel will be subject, which may compromise the entire RWS. Also, there are some constrains to consider.

- *Inertial constrain*: It will be assumed the non-optimized RWS configuration (worst case) in which each of the three wheels are aligned with the X,Y and Z axes w.r.t. the satellite fixed-body reference frame. Consequently, each wheel should be able to store angular momentum over a dynamic range of $H_{req} = 1.09 \times 10^{-3}$ Nms. The value for H_{req} takes into consideration the integration of the maximum disturbing torque magnitude caused by any external forces acting on the satellite, as well as the necessary angular momentum that should be transferred to the satellite in order to maintain the required attitude during its manoeuvre above Victoria, B.C., which takes approximately 400 seconds to complete (see Fig. 1.4). Thus, according to Eq.2.14, the inertia momentum of the flywheel w.r.t. the wheel spin axis $I_{zz_{wheel}}$ shall be bigger than 5.533×10^{-7} kg.m^2.

$$I_{zz_{wheel}} \geq H_{req}\frac{30}{\pi n} - I_{zz_{motor}} \tag{2.14}$$

  where n is the nominal angular velocity of the flywheel, which accordingly to 2.1.3 should be 18400 rpm.

- *Geometric constrain*: It was defined that the difference between the internal radius of the disk, R_i, and the external radius of the rim, R_0, should be bigger than $2\ mm$, in order to facilitate the manufacture of the flywheel;

Another factor to consider relates with the selection of the best material to be used in the construction of the flywheel.

After several analysis to different materials with distinct proprieties, such as density, young modulus, maximum shear stress and its applications to the aerospace industry, it was concluded that aluminium and copper are the main desirable materials to be used [23, 29]. Throughout this section it will be shown that aluminium has a better performance than copper, not only because it is a lighter material, but also due to its mechanical properties.

Now, by using a linear multi-objective optimization problem (MOOP) it is possible to determine the right parameters for the design of the flywheel. For a given system, the Pareto frontier or Pareto set is the set of parametrizations (allocations) that are all Pareto efficient, ı.e. a state of allocation of resources in which it is impossible to make any one individual better off without making at least one individual worse off.

Finding Pareto frontiers is particularly useful in engineering. By yielding all of the potentially optimal solutions, it is possible to make trade-offs within this constrained set of parameters, rather than needing to consider the full ranges of parameters [30].

The following feasible objective space graph (see Fig. 2.4) shows several solutions for the problem. However, the optimal solutions are all located in the Pareto-optimal front (in red). It was also considered that both of the objective functions have the same weight, which results in the marked optimal solution for each material.

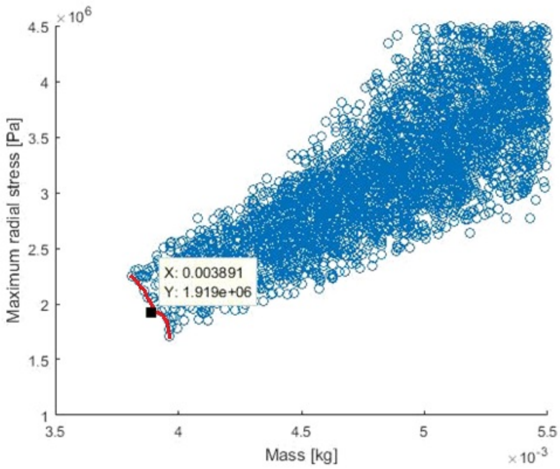

(a) Aluminium

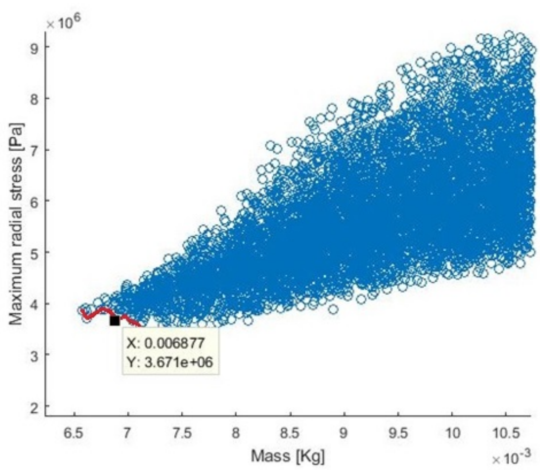

(b) Copper

Figure 2.4: Feasible objective space

In summary, it is easy to conclude by analysing both of the aforementioned graphs that aluminium is a much more desirable material than copper due to its weight and by the reason that a flywheel made from aluminium will suffer a smaller maximum radial stresses. For this reason, hereinafter, aluminium is the only material that is going to be considered in the analysis.

2.2.4 The real flywheel

In the real flywheel a hub around the axis of rotation shall be considered in order to mount the shaft to the flywheel and to serve as a reinforcement of the disc, see Fig. 2.5. The thickness of the hub will be defined as 1 mm.

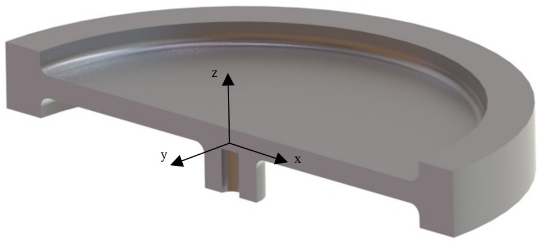

Figure 2.5: Computational model of the real flywheel [SolidWorks©]

Moreover, the real flywheel will also display another difference in the geometry when compared to the theoretical disk-rim flywheel. This difference relates to the use of fillets. It was defined that each fillet shall have a radius of 0.5 mm. This value was set in order to facilitate the manufacture of the flywheel and simultaneously reduce the stress accumulation in these areas.

After selecting the material and by using the pareto optimal solution, the best values for each design parameter that minimizes the mass and the maximum radial stress of the flywheel was obtained, see Fig.2.6. All the results were rounded to a precision of 0.5 mm in order to promote an easier and less expensive manufacture of the flywheel. The properties of the flywheel, namely the moments of inertia around each axis w.r.t. the flywheel's reference frame, as well as its mass were determined using SolidWorks© (see Appendix. B).

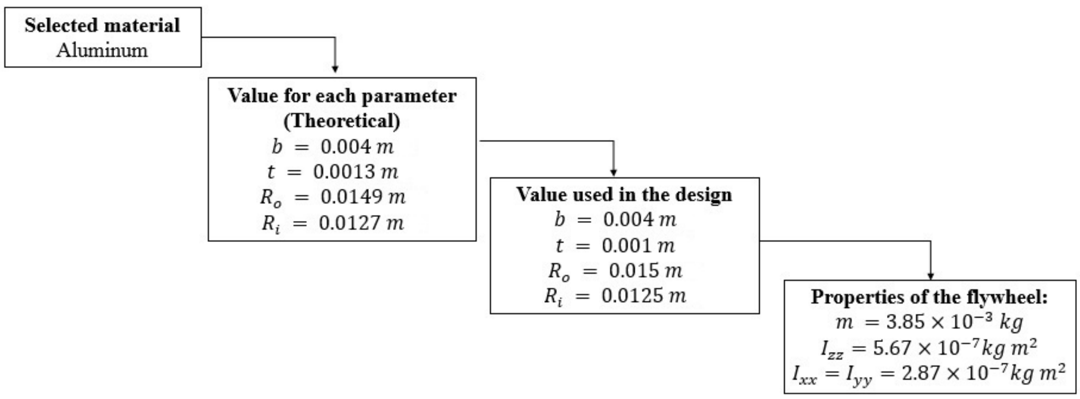

Figure 2.6: Flywheel's design chart

2.2.5 Comparative analysis

As it was already verified the real flywheel design fulfils all the specified requirements namely the inertial and geometric constrains. Moreover, the use of the optimal Pareto-front has enabled to determine the best solution for the minimum mass and simultaneously maximum radial stress.

After setting the parameters in which the flywheel was based it was important to verify if the results based on the theoretical model for the flywheel are in accordance with the ones obtained for the real flywheel. In order to made such verification a structural analysis, using ANSYS Workbench, were performed in order to determine the maximum radial stress the structure was subject at different rotational velocities. After modulated the flywheel in ANSYS Workbench a ten-noded tetrahedral element (tet10) was selected, having the mesh an element size of 1.5×10^{-4} m. This allow the validation of the results obtained by using the theoretical disk-rim flywheel's simplified design.

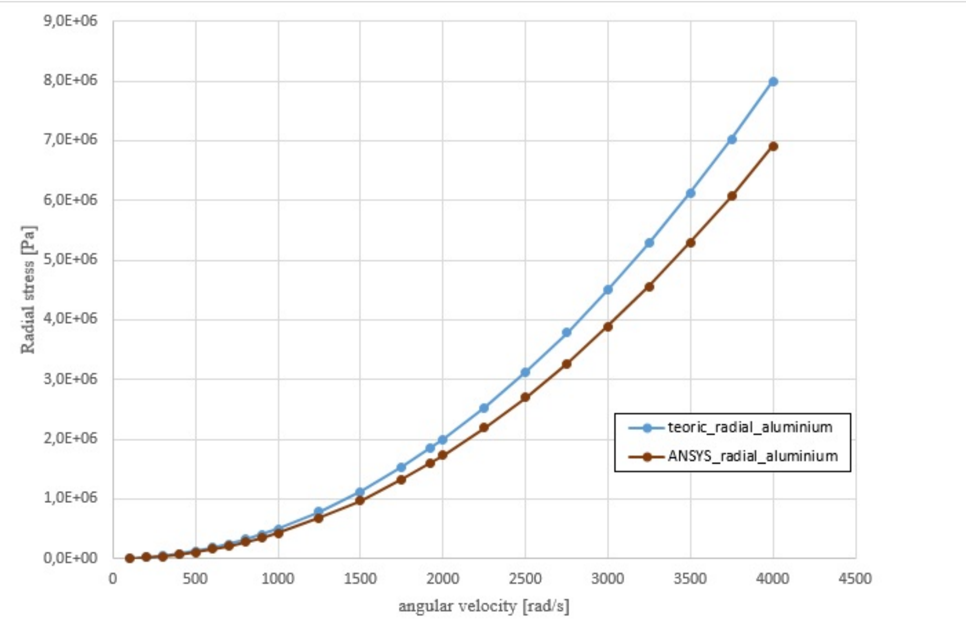

Figure 2.7: Maximum radial stress [Pa] for different rotational velocities [rad/s] computed theoretically and by using ANSYS Workbench software

Based on the previous graph, Fig. 2.7, it was possible to verify that the theoretical results expected were different than the ones obtained by ANSYS Workbench. The computed values using ANSYS Workbench were 13.35% smaller than the theoretical ones and this difference is independent of the rotational speed of the wheel. It was also noticed that if the hub and the fillets previously described were neglected the difference between the theoretical and the computational values were only 4%. Thus, it can be assumed that this difference is mainly justified by the reinforcement caused by the hub and the fillets that were applied to the structure. Moreover, the value for the maximum radial stress obtained theoretically are always bigger than the ones obtained computationally, which for preliminary design proposes can be used as an upper bound for maximum radial stress over which the flywheel is subject.

Consequently, it is possible to conclude that the method developed along this section is good, fast and simple enough to be implemented for project and preliminary design proposes of a disk-rim flywheel in which the main objective is to minimize the mass of the flywheel, as well as the radial and tangential stresses.

It is not only important to define the radial and the tangential stress, but to determine if the structure will yield when subject to that stresses. A yield strength or yield point of a material is defined in engineering and materials science as the stress at which a material begins to deform plastically. Prior to the yield point the material will deform elastically and will return to its original shape when the applied stress is removed. Once the yield point is passed, some fraction of the deformation will be permanent and non-reversible. One good way to determine if the material starts to yield is by using the von Mises yield criterion, which is formulated in terms of the von Mises stress or equivalent tensile stress [31]. This criterion is very well known in industry and it will be used to test the reliability of the structure. After all, if the material starts to yield, the provided torques by the RWS system will be impossible to determine and the entire system would, consequently, be inoperative. Aluminium as a tensile yield strength of 414 MPa, which is far bigger than the value for the von Mises stress at which the structure will be subject, see Fig. 2.8. Thus, no yield of the material will occur.

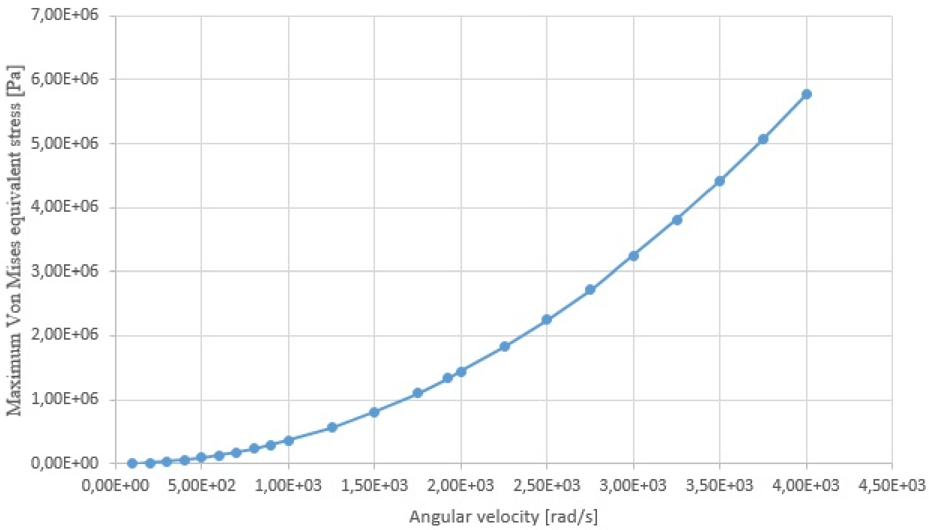

Figure 2.8: Maximum Von Mises equivalent stress [Pa] relative to the angular velocity of the flywheel [rad/s]

2.3 RWS Configuration

In the previous sections it was assumed a standard configuration of three wheels each one aligned with the body X,Y and Z axes of the satellite w.r.t. the fixed-body reference frame. This was done in order to ensure each wheel would be capable to deliver the required torque into each axe of the satellite. However, that configuration has a fundamental problem, since there is no redundancy in the RWS. Hereupon, a detailed analysis of the arrangement of the RWS, considering not only the redundancy of the system but also the minimization of the power consumption is going to be done.

A good way to start setting the actuators in the satellite is to align each actuator along each principal body axis of the satellite to provide full three-axis control authority and maximize torque capability [32, 33]. However, due to redundancy reasons a fourth wheel is normally added to maintain full 3-axis controllability when one wheel fails [13]. There is a NASA standard configuration already tested that could be used. In this configuration a fourth skewed wheel is added, such that its axis is equally inclined from the three orthogonal reference axes [34].

Considering more recent investigations in these field there are other configurations that can have better performance. Pyramidal configuration is an approach that can be considered as a specific arrangement of actuators in satellites and attitude simulators [32].

Harushisa Kurokawa [35] showed that the pyramid type is one of the most effective candidate torquer for attitude control, having such advantages as a simple mechanism and a larger angular momentum space. In that study it was also concluded that if the skew angle of pyramidal arrangement is $\tan^{-1}(1/2)$, then the size of the workspace, ı.e. the region allowed for the angular momentum vector, along the three axis is almost identical, meaning this configuration therefore gives the maximum unidirectional workspace size [35].

Nevertheless, there are several factor in the RWS configuration that should be consider to optimize the entire system. One of the design criteria of this system is to minimize the power consumption of the system during the attitude manoeuvre, specially the one that is going to be performed above Victoria, BC.

Obviously, choosing a proper skew angle will lead to achieve minimum power consumption, which is the objective to be achieved in the ECOSat-III RWS configuration. Also, other criteria such as maximum rotational speed of the wheels can be assumed as the main goal in this optimization, as well as the rotation necessary, without going into saturation, to maintain the angular momentum if one of the four wheels fails [32]. However, this last described criteria are not going to be taken into consideration.

It was verified that the standard configuration proposed by NASA can not be used with the selected motor. For instance, if the wheel aligned with the body y+ axis fails the system will be overloaded, ı.e. the other wheels to maintain the desired attitude will enter into saturation before the conclusion of the desired manoeuvre (in less than 400 s, which is the time required to perform the manoeuvre described in Chapter 1). In sum, maximum rotational velocity for each wheel will be reached in a very narrow time when compared to other configurations.

Thus, hereinafter only the pyramidal reaction wheel arrangement is going to be considered, not only due to its redundancy, but also due to the time it takes, in case one of the wheels fail, for the system to enter into saturation (see Section. 4.7).

2.3.1 Pyramid configuration

Along this section the pyramid configuration shall be studied in order to determine which arrangement shall be the best in terms of power consumption.

The direction of each spin axis can be flipped, but it is defined intentionally, as shown in Fig. 2.9. The reason why this was defined in such way, relates to the fact that it enables to reduce the perturbations caused by each motor and simultaneously make a null vector of the torque generated during the stabilization of the RWS around the nominal speed after the switch on of the satellite in orbit. This reason will be better analysed and understood in the following Sections.

Moreover, it will be implicitly assumed that all the reaction wheels on the spacecraft are identical, which is usually, but not universally the case. However, for ECOSat-III mission each reaction wheel is going to be construct exactly in the same way.

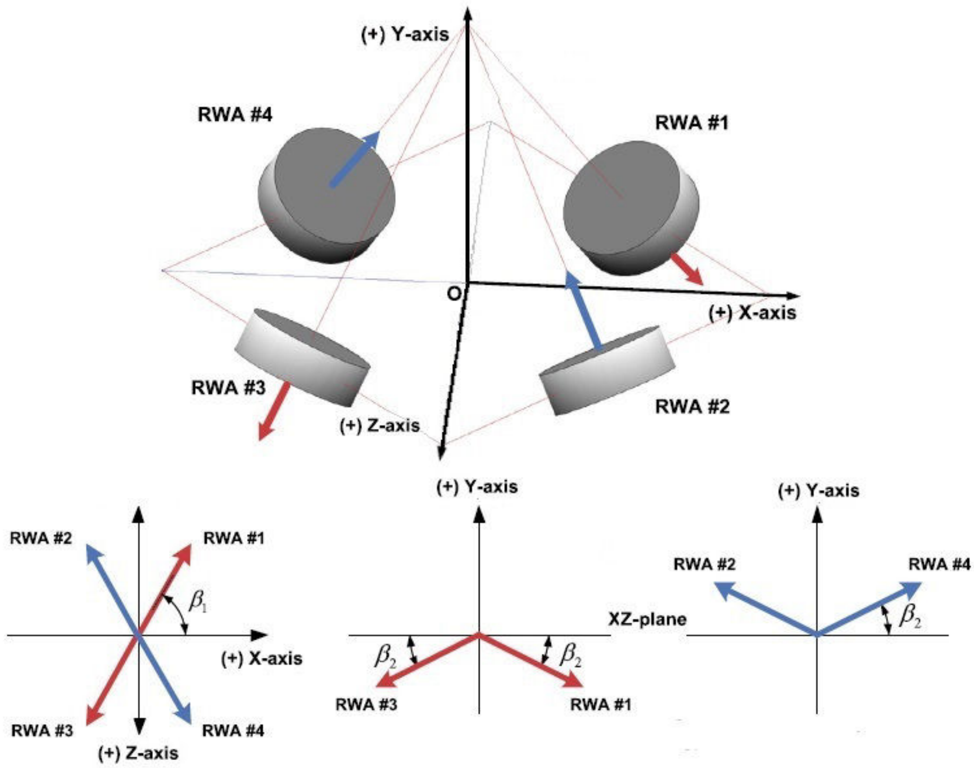

Figure 2.9: Reaction Wheel array in the pyramid configuration [32]

Assuming the configuration aforementioned, see Fig.2.9, it is possible to arrange the applied wheel angular momentum of the individual wheels in a column vector $H_w = [H_1 H_2 H_3 H_4]^T \in \Re^4$, where the subscript W denotes the n-dimensional wheel frame. The transformation from the wheel frame to the body frame is given by the 3×4 distribution matrix W, whose columns are unit vectors in the body frame w_i, along the spin axes of the wheels [36]:

$$W = [\widehat{w_1}, ..., \widehat{w_4}]_{3\times 4} \tag{2.15}$$

Thus, the total angular momentum generated by the RWS is $H_t \in \Re^3$ and are related with the angular momentum of each individual wheel according to

$$H_t = W H_w, \tag{2.16}$$

and the torque relationship can be written as

$$T_t = W T_w, \tag{2.17}$$

where $T_t \in \Re^3$ is the total torque and $T_w = [T_1 ... T_4]^T \in \Re^4$ is the torque vector of the wheel array. Thus, assuming the specific configuration shown in Fig. 2.9, the distribution matrix W can be expressed as,

$$W = \begin{bmatrix} \cos\beta_1\cos\beta_2 & -\cos\beta_1\cos\beta_2 & -\cos\beta_1\cos\beta_2 & \cos\beta_1\cos\beta_2 \\ -\sin\beta_2 & \sin\beta_2 & -\sin\beta_2 & \sin\beta_2 \\ -\sin\beta_1\cos\beta_2 & -\sin\beta_1\cos\beta_2 & \sin\beta_1\cos\beta_2 & \sin\beta_1\cos\beta_2 \end{bmatrix} \tag{2.18}$$

Based on the transformation matrix, W, presented in Eq. 2.18 it is possible to determine the velocity each wheel should rotate in order to maintain the required angular angular momentum of the satellite during a specific manoeuvre.

It will be assumed all the angular momentum generated by the RWS is transmitted to the satellite. As it was already specified the major variation on the angular momentum will occur above the Island of Vancouver, as mentioned in Chapter 1.

2.3.2 Power analysis

After defining the pyramid configuration as the one that is going to be used, the goal is now to find the optimal angle β_1 and β_2 that minimizes the power consumption.

This configuration will be optimized for the manoeuvre above the Vancouver Island. In this, the y-axis of the RWS should be aligned with the body y-axis of the satellite, since this is the axis, over which the system shall have the biggest manoeuvrability.

The variation of the total angular momentum of RWS is determined by integrating the torque that shall be delivered to each axis of the satellite (see Chapter 1) over the manoeuvre time, which takes approximately 400 seconds.

Thus, the variation of the total angular momentum generated by the RWS during the manoeuvre above Victoria, BC, should be $\Delta H_t = [4.88 \times 10^{-4}; 1.091 \times 10^{-3}; 4.88 \times 10^{-4}]$ Nms. The values for ΔH_{t_x} and ΔH_{t_z} correspond to the variation of the total angular momentum if only the external perturbation torques were considered acting on these axes during the aforementioned manoeuvre.

Based on the variation of the total angular momentum it is possible to determine the angular momentum variation of each individual wheel,

$$\Delta H_w = W^{\dagger} \Delta H_t, \tag{2.19}$$

where the superscript † denotes the pseudo-inverse matrix of W. It was assumed that each wheel had an initial rotational velocity of 18400 rpm. By knowing the variation of the angular momentum of each wheel, it is now trivial to determine the final rotational velocity of each wheel,

$$\Delta H_w = \Delta w_w I_w, \tag{2.20}$$

where $I_w = [I_1 ... I_4]^T \in \Re^4$ which corresponds to the inertia momentum of each wheel around the spin axis. By using the relations developed in Section 2.1.3 the power consumption was determined for different values of β_1 and β_2.

In sum, the determination of the power consumption was done by using the variation of the total angular momentum. Based on that, it was possible to determine the final angular velocity of each wheel assuming the simplified DC model described in Chapter 1, which are related with the necessary voltage to be provided to each motor. Several simulations to different β_1 and β_2 angles were performed in order to determine the configuration that generates the lowest power consumption, see Fig. 2.10.

Based on the graph presented in Fig. 2.10 it was possible to conclude that the best configuration which minimizes the power consumption for the required manoeuvre implies that $\beta_1 = 45°$ and $\beta_2 = 60°$.

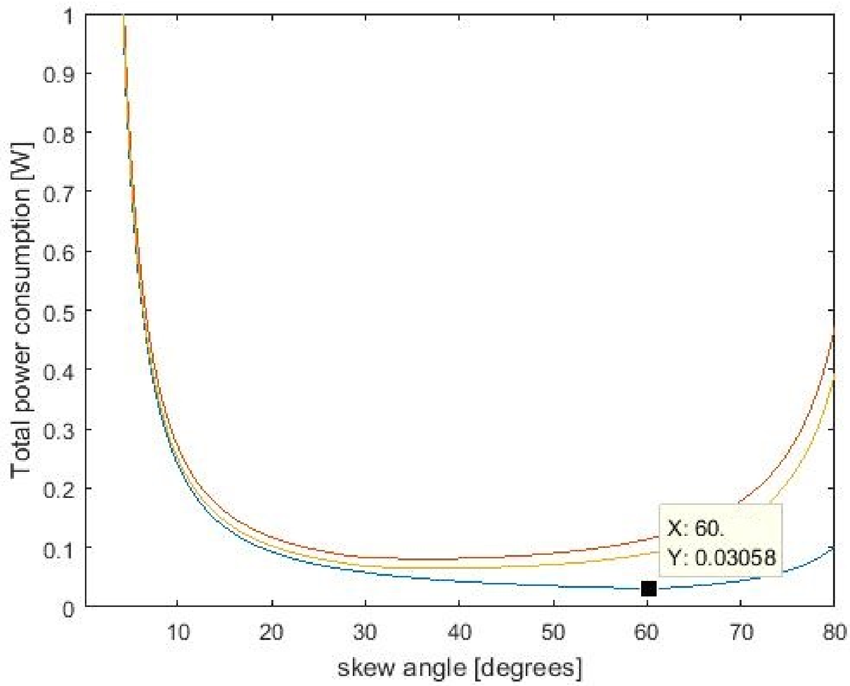

Figure 2.10: RWS power neglecting the electronics power consumption as function of the skew angle. ($\beta_1 = 45°$ in blue; $\beta_1 = 40°$ in green; $\beta_1 = 50°$ in red). Minimum power consumption for $\beta_1 = 45°$ and $\beta_2 = 60°$

Chapter 3

Reaction Wheel Internal Disturbances

Disturbance torques and disturbance forces acting on the motor are of special concern because they potentially have a great impact on other subsystems too. There is also other concern that should be considerered which relates to the fact that the RWS could not be perfectly aligned with respect to the satellite's principal axes. This misalignment does not result in periodic disturbances and its effect can be described as a torque off-set [23]. However, its analysis shall be made after the conclusion of the structural design and setting its location inside ECOSat-III, which was not yet defined. Nevertheless, along this thesis it was assumed to be in the center of mass of the satellite.

Hereupon, in this Chapter only periodic disturbance forces and torques from the RWS are going to be discussed, since this would be more severe and difficult to control, if necessary.

3.1 Sources of disturbances

There are two main disturbances that may affect the dynamics of the RWS. Both of them should be analysed in order to determine if they can disturb the entire system and finally a method to solve this disturbances will be analysed if it has a visible impact on the satellite performance. The main sources of this internal disturbances are [23],

- **Axial play in the shaft of the motor**. From the specifications of the selected COTS motor - FAULHABER 1202 004 BH, the axial radial play in the motor axle, δ_{play}, will have a value of 0.011 mm at the bearing exit. Again according with the specification the distance between the origin of the motor and the bearing exit, $d_{bearing}$ is about 0.074 mm. Thus, according to this data the maximum deflection of the motor's shaft is given by,

$$\theta_{axle} = \tan\left(\frac{\delta_{play}}{d_{bearing}}\right). \tag{3.1}$$

- **Flywheel manufacturing tolerances**. Its impossible to create a perfect manufactured material with a uniform density distribution. Thus, it will be assumed that the center of mass of the real flywheel will have a shift in relation to the perfect model. This shift for simplicity is going to be caused due to tolerance manufacturing errors. The errors caused by a non-uniform density distribution of the material that compose the flywheel is going to be neglected. Hence, the density distribution is going to be considered uniform. This manufacturing error will be represented by an angle which correlates the tolerance in the width of the rim with the deflection of the center of mass [23]. This angle is obtained assuming a variation in the flat feature of $\delta_{tolerance} = 0.01$ mm

$$\theta_{man} = \tan\left(\frac{\delta_{tolerance}}{r_{wheel}}\right). \tag{3.2}$$

The following Fig.3.1, shows how the sources of this internal disturbances will deflect the flywheel relatively to a perfect RWS model.

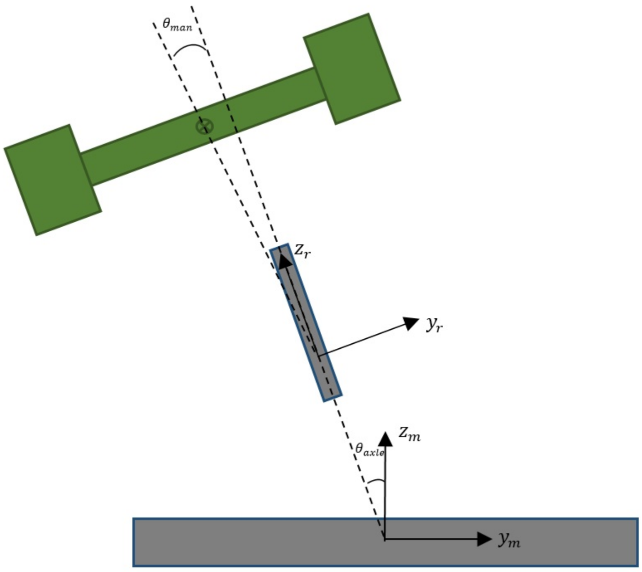

Figure 3.1: Deflection angles representation due to internal disturbance torques sources in the Reaction Wheel

This deflection of the rotation axis will create a torque that is going to act in the RWS. This torque is caused due to the gyroscopic effect and it should be analysed how the magnitude and the frequency of the generated torque will be reflected in the response of the all system. In this Chapter it will be assessed the effect these error angles may have in the RWS. The major objective to compute is the resulting worst-case accelerations of the flywheel with respect to the origin of the body-fixed motor reference frame.

3.2 Induced disturbances

3.2.1 Mathematical representation

The objective here is to assess the acceleration of the flywheel center of gravity in the body-fixed reference frame. Thus, the position vector of the flywheel center of gravity, r_w^M, expressed in the body-fixed motor reference frame is given by,

$$r_w^M = r_o^M + R^{M/R} r_w^r, \tag{3.3}$$

where r_o^M is the position vector from the body-fixed motor reference frame origin to the origin of the rotor reference frame. The motor reference frame origin is considered to be in the geometric center of the motor's cage, i.e. 0.74 mm above its base and the origin of the rotor reference frame is considered to be 1 mm above the base of the motor shaft. Assuming this, $r_o^M = [0; -z_o sin(\theta_{axle}); z_o cos(\theta_{axle})]$, where $z_o = 1.74$ mm is the distance to the flywheels base relative to the origin of the motor reference frame. The variable r_w^r is the position vector from the origin of the rotor reference frame to the flywheel center of mass expressed in the rotor reference frame. This vector is written as, $r_w^r = [0; -z_w sin(\theta_{man}); z_w cos(\theta_{man})]$, where $z_w = 2.477$ mm is the distance from the origin the rotor reference frame (flywheel's base) to the flywheels center of mass. This value was obtained using ANSYS Workbench. The rotation matrix $R^{M/R}$ transforms a vector expressed in the rotor reference frame in the motor reference frame.

$$R^{M/R} = \begin{bmatrix} 1 & 0 & 0 \\ 0 & \cos\theta_{axle} & -\sin\theta_{axle} \\ 0 & \sin\theta_{axle} & \cos\theta_{axle} \end{bmatrix} \tag{3.4}$$

Nevertheless, it shall be consider that the motor is rotating around its Z-axis with speed ω, which will affect the temporal evolution of the acceleration vector in the motor reference frame. Thus, a time-dependent transformation matrix $R^{\omega t}$ shall be added to Eq. 3.3.

$$R^{\omega t} = \begin{bmatrix} \cos\omega t & \sin\omega t & 0 \\ -\sin\omega t & \cos\omega t & 0 \\ 0 & 0 & 1 \end{bmatrix} \tag{3.5}$$

This means Eq. 3.3 shall be re-written as

$$r_w^M = r_o^M + R^{M/R} R^{\omega t} r_w^r. \tag{3.6}$$

The instantaneous velocity of the flywheel center of gravity with respect to the motor origin is obtained by taking the derivative of Eq. 3.6:

$$v_w^M = \frac{dr_w^M}{dt} = \dot{r}_o^M + \Omega \times r_o^M + R^{M/R} R^w \dot{r}_w^r + \Omega \times (R^{M/R} R^w r_w^r). \tag{3.7}$$

Thus assuming that $\dot{r}_o^M$ and $\dot{r}_w^r$ are fixed in time within their respective reference frames, Eq. 3.7 can be simplified to:

$$v_w^M = \Omega \times r_o^M + \Omega \times (R^{M/R} R^w r_w^r) = \Omega \times r_w^M. \tag{3.8}$$

The instantaneous acceleration of the center of gravity in the body-fixed motor reference frame can then be expressed by taking the first derivative of Eq.3.8

$$a_w^M = \frac{dv_w^M}{dt} = \dot{\Omega} \times r_w^M + \Omega \times \dot{r}_w^M + \Omega \times \Omega \times r_w^M. \tag{3.9}$$

Since $\dot{r}_w^M$ is fixed in time, Eq. 3.10 will be simplified as,

$$a_w^M = \frac{dv_w^M}{dt} = \dot{\Omega} \times r_w^M + \Omega \times \Omega \times r_w^M, \tag{3.10}$$

where,

$$\dot{\Omega} = \begin{bmatrix} 0 \\ -\dot{\omega} \sin\theta_{axle} \\ \dot{\omega} \cos\theta_{axle} \end{bmatrix}, \tag{3.11}$$

$$\Omega = \begin{bmatrix} 0 \\ -\omega \sin\theta_{axle} \\ \omega \cos\theta_{axle} \end{bmatrix}. \tag{3.12}$$

Again, assuming that the origin of the motor reference frame is the pivot point of the motor axle, the angular acceleration can be easily defined by

$$\alpha_w^M = r_w^M a_w^M. \tag{3.13}$$

Disturbance torques

With the disturbance force applied on the flywheel center of gravity, the disturbance torque, T^{fw}, acting on the motor reference frame origin can be calculated,

$$T^{fw} = I_w^M \alpha_w^M, , \tag{3.14}$$

where I_w^M represents the inertia tensor of the flywheel w.r.t. the body-fixed motor reference frame. However, there is only data available for the moment of inertia tensor of the flywheel w.r.t. the body-fixed flywheel reference frame. Thus, a transformation of the inertia tensor shall be considered. For simplicity the moment of inertia of the motor will be neglected. This implies that,

$$I_w^M = R^{M/R} R^{wt} (R^{R/fw} I_{fw} (R^{R/fw})^t + I_{r_w^r})(R^{M/R} R^{wt})^t + I_{r_o^M}, \tag{3.15}$$

where I_{fw} is the diagonal inertia matrix in which its components were determined in Section. 2.2.4; $R^{R/fw}$ is the transformation matrix that transforms the inertia tensor expressed in the flywheel's reference frame in the rotor reference frame; $I_{r_w^r}$ is the additional moment of inertia due to the translation of the reference frame from the flywheels center of mass to the rotor reference frame and similarly $I_{r_o^M}$ is the additional moment of inertia due to the translation of the reference frame from the rotor reference frame to the motor reference frame. The index ^{t} denotes the transpose matrix.

According to Eq. 3.14, it is easy to conclude that the magnitude of the disturbing internal torque is proportional to the rotational speed of the wheel (see Fig. 3.3).

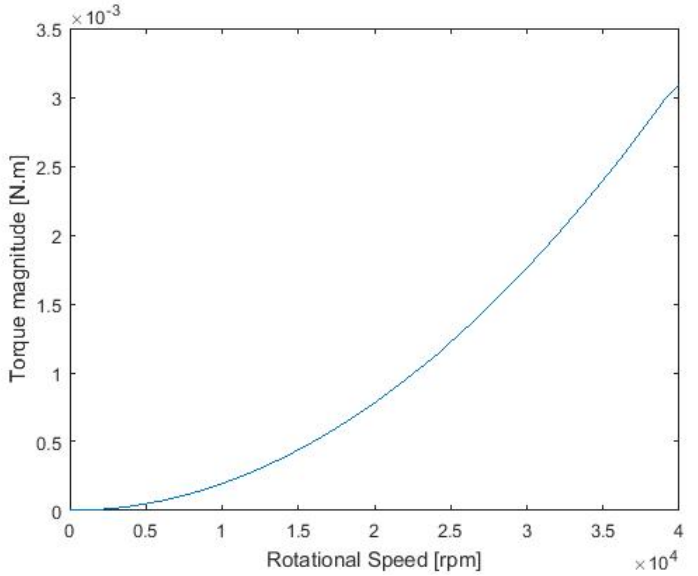

Figure 3.2: Magnitude of the disturbing torque as function of the velocity

It was verified, this magnitude as expected increases with the rotational speed of the flywheel. It was also possible to conclude that the disturbing torques caused by the axial play on the shaft of the motor and due to imperfections on the manufactured flywheel, will generate a harmonic disturbing torque two orders of magnitude bigger than the required torque needed to control the satellite (see Fig. 3.3, which describes these disturbing internal torques for a rotation speed of $18400\ rpm$).

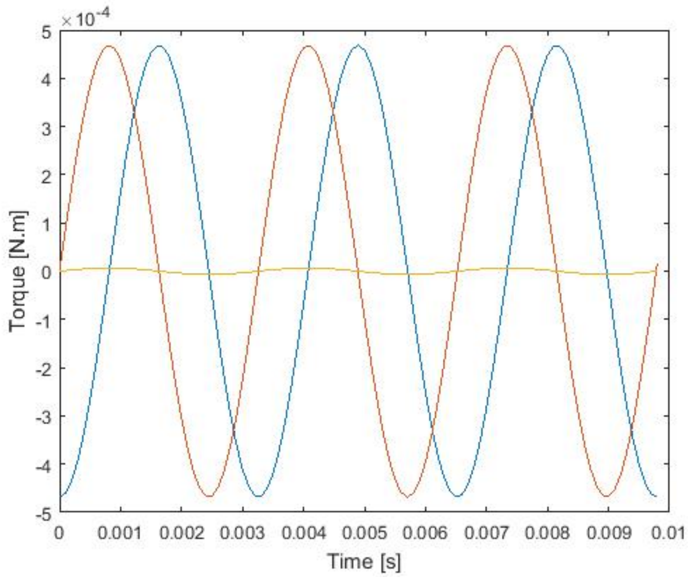

Figure 3.3: Internal disturbing torques caused by one wheel rotating at $18400\ rpm$. (Red, Blue, Green) - disturbing torque component in the X, Y, Z direction in the body-fixed motor reference frame, respectively

From the data expressed in Fig. 3.3 it was possible to conclude that the magnitude of the torque in the X and Y direction is two orders of magnitude bigger than the disturbing torque on the Z directions.

Nevertheless, the disturbances on the Z direction shall not be, in any case ignored, since it will have an impact on the torque/speed curve despite the harmonic characteristics of the disturbance.

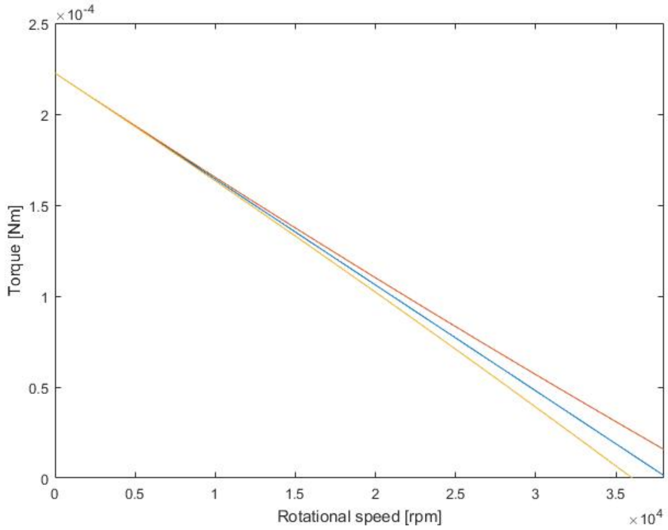

Figure 3.4: Torque/speed curve of the motor without the flywheel (blue) and respectively the upper (red) and lower (blue) torque/speed bound considering the flywheel

In Fig. 3.4 it was shown the maximum and the minimum limits of the torque in the torque/speed curve in order to verify the possible variation on the results expected with and without the flywheel coupled on the selected motor.

This lower and upper bounds should be later verified through experiments. However, this topic here discussed shows that the coupled flywheel will definitely influence the motor response. It was also verified that the value of $\delta_{tolerance}$ will have an huge impact on the magnitude of the disturbing torque generated, meaning that higher manufacturing precision, i.e. smaller tolerances, will cause a reduction in the magnitude of the disturbing internal torque. By intentionally neglecting this problem, it will be later shown that the internal disturbing forces acting on the RWS will have a negligible impact on the satellite. This means that no higher manufacturing tolerance precision would be needed.

Then, the modulation of the all RWS internal disturbances, and consequently the definition of its dynamics, become more complex. This is not only caused due to unpredictable behaviour (which is not going to be considered in this thesis), but also due to the difficulty to determine the initial phase of each disturbance component induced by each wheel.

Despite having uncertainties about the phase of each initial disturbing torque, a simple modulation can be done assuming a random shift on the phase between each disturbing torque component. Based on the optimum RWS configuration it is possible to determine the induced torque on each axis of the body-fixed satellite reference frame by the RWS.

Assuming perfect conservation of the angular momentum, all the torque generated by the RWS will be transferred to the satellite.

To assess the impact of the disturbance torque on the satellite the maximum angular displacement relatively to its desired pointing position, caused by this internal disturbances, shall be determined.

Thus, the angular displacement around the $y+$ axis w.r.t. the satellite's body-fixed reference frame shall be determined, since any angular displacement around this axis will have a bigger impact on the satellite pointing precision than the angular displacement generated around the other axes. First the total disturbance torque is converted into corresponding angular acceleration vector of the satellite, assuming all the torque generated by the RWS was transferred to the satellite. The double integration over time of this parameter will assent to determine the maximum angular displacement, δ_{sat}, relatively to the pointing position that the satellite will suffer when the RWS is activated and the wheels rotate at a certain speed,

$$\delta_{sat} = \int \int (I_b)^{-1} T^{fw} dt. \tag{3.16}$$

To verify this disturbances it is going to be assumed that all the reaction wheels are rotating at a random speed, between 5000 and 20000 rpm. Assuming the previous described operating mode, and a random value for the phase perturbation component of each wheel, it is possible to draw a scheme of the angular displacement of the satellite around the y-axis w.r.t. the satellite body-fixed reference frame (see Fig. 3.5).

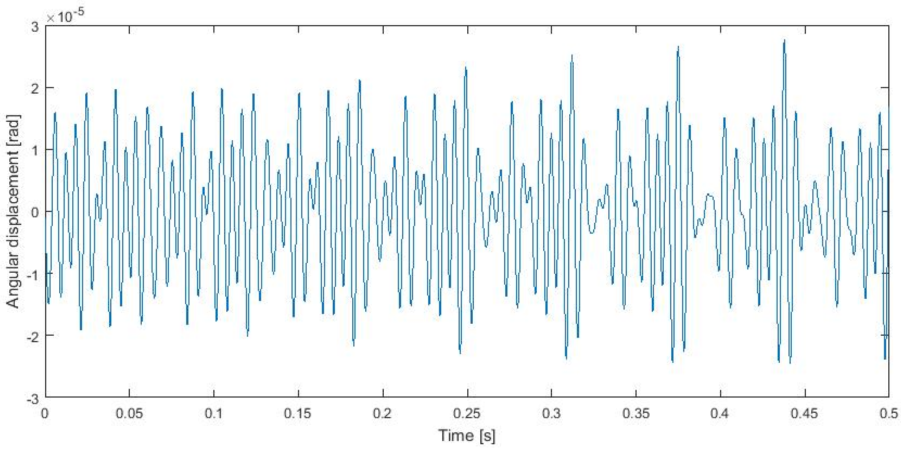

Figure 3.5: Angular displacement of the satellite around the y-axis w.r.t. the satellite body-fixed reference frame

3.2.2 Modelled results

The results obtained in this section have showed that despite their significant magnitude, these disturbances are not likely to affect the mission performance. The disturbances induced by the RWS greatly exceed the required maximum value and their amplitude is directly related to the reaction wheel rotation speed. At 18400 rpm the calculated amplitude of the resulting disturbance torques is in the order of magnitude of 10^{-3} Nm, whereas the maximum external disturbance torques are in the order of magnitude of 10^{-6} Nm.

Then, a first analysis may lead to conclude that the internal disturbances caused by the RWS will make its use impossible. Nevertheless, since the disturbances originated by the RWS are periodic, the absolute impact on the satellite attitude will be negligible. This is confirmed by Fig. 3.5, which shows that, at a random velocity of rotation for each wheel, the impact of the angular displacement of the satellite relatively to the desired point can be negligible. Moreover, the pointing precision required for ECOSat's mission is approximately $2°$, which is bigger than the maximum oscillation induced in the satellite by this disturbing internal forces - about 10^{-3} degrees, meaning there is no need to increase the controllability of this system. This confirms that the effect of this disturbance forces can be considered negligible.

Chapter 4

Control of the Reaction Wheel System

BLDC motors have been used in different applications, such as industrial automation, automotive, aerospace, instrumentation and appliances since 1970's [37]. BLDC motor is a type of DC motor where its commutation is done electronically instead of using brushes. Therefore there is a need of less maintenance. Moreover, electronic commutation technique and permanent magnet motor cause BLDC to have immediate advantages over brushed DC motor and induction motor in several electric applications [38].

In this section the overall system model is going to be explored, as well as its response to a desired input. Subsequently a close-loop PID controler will be designed. The designed model shall be integrated on the Attitude Control and Determination System (ADCS) of ECOSat-III. Then, a fast and precise torque and velocity control is the major objective for the RWS.

BLDC motor has more complex control algorithm compared to other motor types due to electronically commutation [37]. Therefore, accurate model of motor is required to have complete and precise control scheme of the BLDC motor. To design a BLDC motor drive system, it is necessary to have a motor model that gives a precise value of torque which is related to the current and back-EMF [39].

4.1 Motor operating principle

A BLDC motor can be also referred to as an electronically commutated motor. There are no brushes on the motor and the commutation is performed electronically at certain rotor positions. The magnetization of the permanent magnets and their displacement on the rotor are chosen in such a way that back-EMF shape is trapezoidal. Thus, the three-phase voltage system, which as a rectangular shape, will create a rotational field with low torque ripples. This, in a certain way means that the BLDC motor is equivalent to an inverted DC commutator motor. In that the magnets rotates while the conductors remain stationary [38]. In a DC commutator motor the current polarity is reversed by the commutator and the brushed. However, in a BLDC, which has no brushes the reversal of polarity is performed by semiconductor switches which must be switched accordingly with the rotor position, using for that the signals originated by the integrated hall sensors [40].

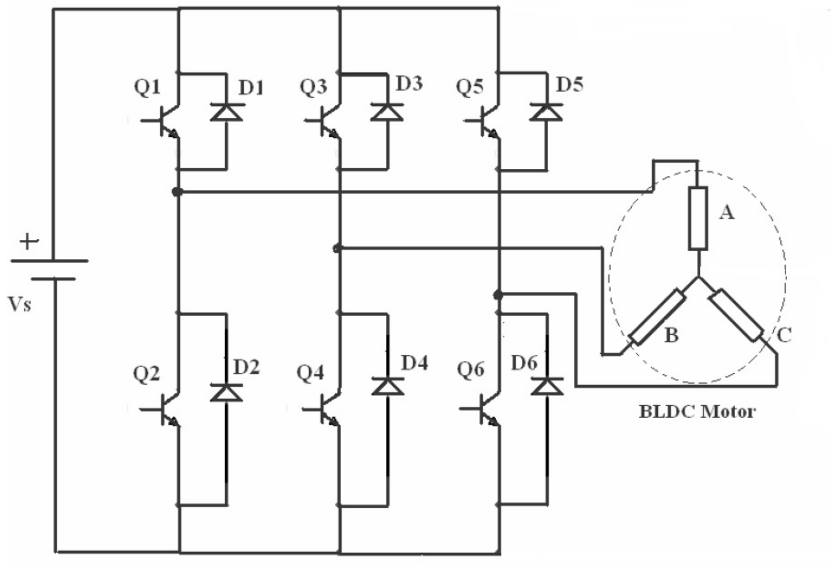

Figure 4.1: Simplified electrical circuit of a BLDC motor

4.1.1 Equation of motion

A BLDC motor can be modulated in a similar manner as a three-phase synchronous machine, but since there is a permanent magnet mounted on the rotor, some of their dynamic characteristics are different [38]. A modelling based on an abc phase variable is more convenient for this motors than using d-q axis [37]. Nevertheless, some assumptions should be made to the model in order to simplify it:

- Magnetic circuit saturation is ignored;
- Stator resistance, self and mutual inductance of all phases are equal and constant;
- Hysteresis and eddy current losses are eliminated;
- All semiconductor switches are ideal and no losses are going to be considered;

Then, the voltage equation of a BLDC motor based on Fig. 4.1 can be expressed as:

$$V_a = Ri_a + L\frac{di_a}{dt} + E_a, \tag{4.1a}$$

$$V_b = Ri_b + L\frac{di_b}{dt} + E_b, \tag{4.1b}$$

$$V_c = Ri_c + L\frac{di_c}{dt} + E_c, \tag{4.1c}$$

where L is the armature self inductance [H]; R is the armature terminal resistance [Ω]; V_a, V_b, V_c are the terminal phase voltage [V]; i_a, i_b and i_c are the motor input current [A] and E_a, E_b and E_c are the back-EMF voltage of the motor for each phase.

In a three-phase BLDC motor, the back-EMF is function of the rotor position and the back-EMF voltage of each phase has $120\deg$ phase different angle difference so equation of each phase should be,

$$e_a = k_w f(\theta_e)\omega, \tag{4.2a}$$

$$e_b = k_w f(\theta_e - 2\pi/3)\omega, \tag{4.2b}$$

$$e_c = k_w f(\theta_e + 2\pi/3)\omega, \tag{4.2c}$$

where k_w is the back EMF constant of one phase [$V/rad.s^{-1}$]

The electrical,θ_e, and mechanical,θ_m, rotor angle can be related by,

$$\theta_e = \frac{p}{2}\theta_m. \tag{4.3}$$

Moreover the $f(\theta_e)$, which is the back-EMF reference function which has trapezoidal shape and maximum magnitude of ± 1 can be represented by,

$$f(\theta_e) = \begin{cases} 1, & \text{if } 0 \leq \theta_e < 2\pi/3 \\ 1 - \frac{6}{\pi}(\theta_e - 2\pi/3), & \text{if } 2\pi/3 \leq \theta_e < \pi \\ -1, & \text{if } \pi \leq \theta_e < 5\pi/3 \\ -1 + \frac{6}{\pi}(\theta_e + 5\pi/3), & \text{if } 5\pi/3 \leq \theta_e < 2\pi \end{cases} \tag{4.4}$$

The total electromagnetic torque output can be represented as the summation that of each phase,

$$T_e = T_a + T_b + T_c, \tag{4.5}$$

where,

$$T_a = K_t i_a f(\theta_e), \tag{4.6a}$$

$$T_b = K_t i_b f(\theta_e - 2\pi/3), \tag{4.6b}$$

$$T_c = K_t i_c f(\theta_e + 2\pi/3), \tag{4.6c}$$

The mechanical dynamic equation of the motor can be now correlated with the electromagnetic torque,

Thus, the mechanical torque provided by the wheel can be expressed by the following equation,

$$Te - T_i = J\frac{d\omega_m}{dt} + \beta\omega_m, \tag{4.7}$$

where J is the moment of inertia of the motor coupled with the moment of inertia of the flywheel [kg.m^2]; β is the dynamic frictional torque constant [Nm/s] and T_i the load torque

Friction Model

A critical point is that, depending on lubrication regime, different surface interaction mechanisms occur, certainly leading to distinct wear and friction responses. In most cases, friction and lubrication relationship is characterized with basis on $\eta V/W$ (oil viscosity x sliding velocity /normal load) factor in a curve called Stribeck diagram, which requires experimental data to determine the friction coefficients [41].

Accordingly to the manufacturer data the friction model to be applied is will be based on a model which assumes the Coulomb friction. The Coulomb friction coefficient is a static force that is slightly higher than motive force when two materials are at rest while in contact with each other [42]. Assuming this as the basis friction model, the friction torque can be described as,

$$T_i = \begin{cases} C_0, & \text{if } n > 0 \\ -C_0, & \text{if } n < 0 \\ 0, & \text{if } n = 0 \end{cases} \tag{4.8}$$

These are reasonable models of friction that could be applied. However, some of the torques generated during near zero rpm are only one order of magnitude smaller than the required torques and have a very random and non-linear behaviour. For this reason it is not preferable for the RWS to operate near the zero rpm. This behaviour can cause considerable attitude errors, and shall have great consequences in the performance of the assigned tasks. Moreover, if the wheels are kept in low rpm range for long, there might be some impact on the wheels reliability [32].

In some actual space programs, specially those involving imaging satellites, the interruption of an imaging mission due to wheel speed zero-crossing should be avoided. Thus, it shall be found an agreement between the reliability and the agility of the RWS. Since this spacecraft is a Cubesat the agility of the RWS does not have priority above the reliability. For such cases, the wheels should be forced to operate only within the half of the speed range without a sign change, ı.e $H_i \in [H_{min}, H_{max}]$ [32]. This scheme is also implemented by setting the nominal speed to half the maximum speed, as considered in Chapter. 1. The value for H_{min} was defined based on the speed below which the RWS starts to lose its non-linear behaviour. This speed was defined as 600 rpm according to the manufacturer.

4.2 Open-loop response

After defining the modelling equations of a BLDC motor a open-loop response analysis shall be made in order to determine the expected results. Unlike a brushed DC motor, the commutation of a BLDC motor is controlled electronically. It should be also considered that a BLDC motor is fed by a three phase MOSFET based inverter, as it can be seen in Fig. 4.1. In this thesis, since there is no information available about the three-H bridge drive that is going to be used, all the losses in the commutation are going to be neglected. The gating signals for firing the power semiconductor devices in the inverter is injected from a hysteresis current controller which is required to maintain the current constant with the 60 deg of one electrical revolution of the motor. This can be obtained using the signals from the hall sensors,

Rotor position (θ_e) [deg]	H1	H2	H3	Switch closed
$0-60$	1	0	0	Q1 Q4
$60-120$	1	1	0	Q1 Q6
$120-180$	0	1	0	Q3 Q6
$180-240$	0	1	1	Q3 Q2
$240-300$	0	0	1	Q5 Q2
$300-360$	1	0	1	Q5 Q4

Table 4.1: Six step switching sequence for commutation

In every 60 deg of rotation, the hall sensor changed its state and each combination of hall sensor states represents a specific rotor position. The BLDC motor uses six step inverter operation for commutation part. This six-step commutation is a relatively inexpensive and cost-effective feedback, where only two windings are energized at a time. Each step rotates at 60 electrical degrees, which six paths make a full 360 degree rotation, meaning only a full 360 degree loop is able to control the current. Consequently, is possible to determine which switches of the MOSFET based inverter are going to be closed in order to modulate the three phase signals. A scheme of the BLDC motor can be observed in Fig. 4.2.

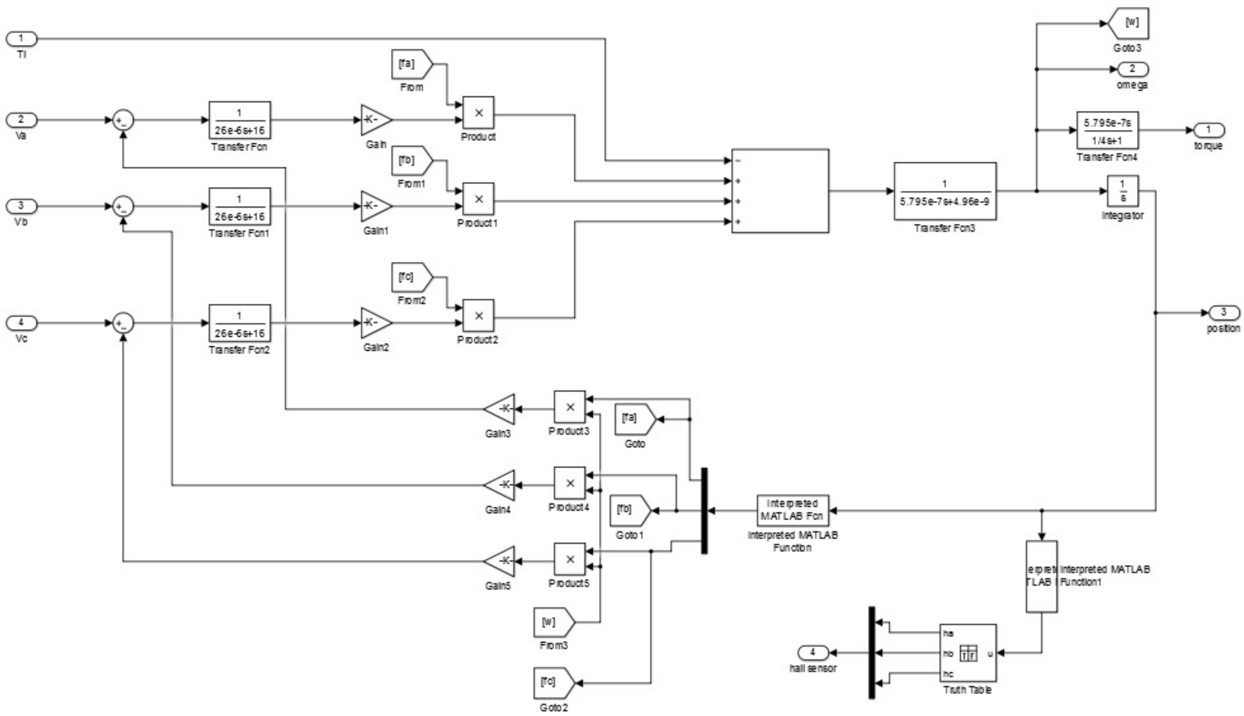

Figure 4.2: BLDC motor simulink block

Here the simulink model has the V_a, V_b and V_c, i.e. the terminal phase voltage of the motor as input, as well as the load torque caused by the static friction due to surface interaction mechanisms, as explained in the previous frictions model. The block named MATLAB function1 is responsible to determine the signal of the back-EMF reference function according to the mechanical motor angle, see Eq. 4.1.1. The simulink block named as MATLAB Function2 is responsible to determine the signals each hall sensor is going to generate in order to perform the six step switching sequence for commutation. In order to simplify the commutation and assuming no losses in the 3-phase H bridge, a full simulink scheme for the brushless DC motor can be designed, see Fig. 4.3

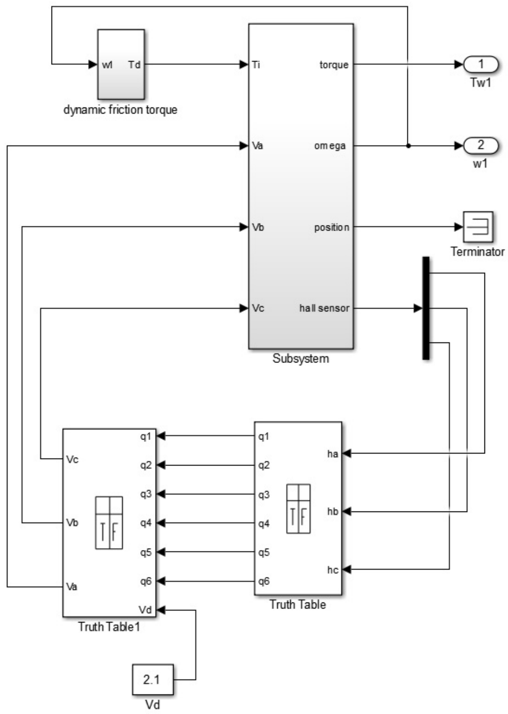

Figure 4.3: BLDC motor drive block

The open loop response of the motor with the designed flywheel can be verified in Fig. 4.4. The input variable is the voltage, which in this case was 2.1 V. As previously determined, see Chapter 1, this voltage input will induce the motor to rotate at a velocity of $18400\ rpm$.

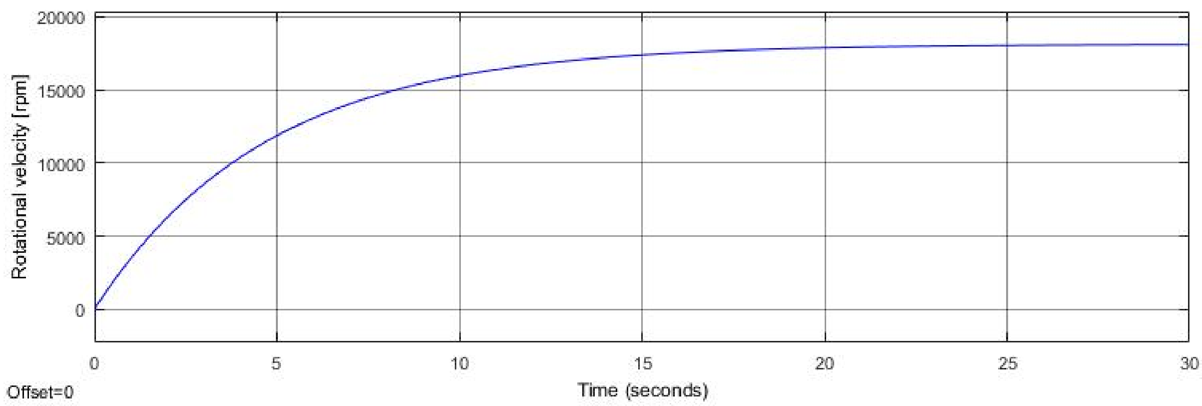

Figure 4.4: Open loop response for an input voltage of 2.1 V

It was also verified that if the value of the static friction torque suffers some deviations form the value specified by FAULHABER the response of the motor for that input will suffer significant changes. Moreover, this value is expected to be modified, based on the fact that the actual lubricant shall be replaced by a vacuum proof lubricant.

Assuming the lubricant is going to be modified the final static and dynamic friction coefficients can be very different from the tabulated values. Thus, a change in the model parameters shall be made in order to adjust the open loop response of the motor. Nevertheless, the aforementioned model is prepared to assume this alterations, and no significant changes, except in the model parameters, have to be made.

4.3 Model validation

In the previous section it was presented a model for a three phase motor that is going to be integrated on the simulation of the ADCS of the satellite in a future phase of the project. In the current phase only a simplified DC motor is going to be considered [43], see Section 4.4. Moreover, the BLDC model shall help to understand the response of the motor to several inputs and determine if the selected actuator components are the desired ones in order to fulfil ECOSat's mission objectives.

National Institute of Technology Karnataka, NITK, India, developed a simulink simulator for a brushless DC motor [44, 45]. This model developed by this faculty team are going to be the basis to validate the simplified model designed in this thesis. To test and validate the previous model a step-size of $0.1\ s$ and an automatic solver selection in both simulations was used. As a matter of fact, the complex model developed by the NITK has a simulation time bigger than the one developed in this thesis. Moreover, only *mybldc block* was used and an adaptation of the commutation drivers were made. In the model developed by NITK the inductance of the motor was neglected contrary to the developed model. This was considered in order to simplify the simulation and decrease the simulation time. Moreover, this model is based in a state-space modelling, which was easily defined based on the information presented in the *User Manual* [45]. The following figure, shows the results for the motor rotational speed over time, for a voltage input of $2.1\ V$. As observed, the response is extremely similar to the one presented in Fig. 4.4, which is the motor's response using the BLDC model developed in this thesis.

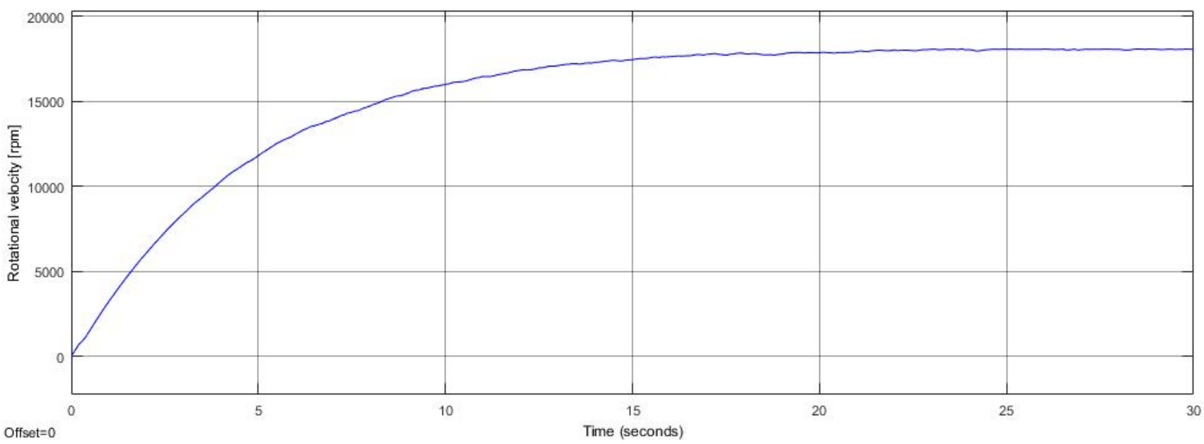

Figure 4.5: Open loop response for an input voltage of $2.1\ V$ - using NITK adapted model

Hereupon, it is possible to conclude the aforementioned model for a BLDC motor developed in this thesis represents a reliable and correct model of the motor that is going to be used in order to characterized the RWS.

4.4 Model implemented in the ADCS

For the ADCS there is no need to observe and analyse the commutation process and the internal currents that flows throughout the BLDC motor. The only important factor was to implement as far as possible the simplest model that gives reliable and realistic output results. This can be achieved by implementing a simplified common DC motor model. Thus, in the ADCS in order to test the overall satellite control system a Simulink model of a DC motor (see Fig. 4.6), based on the Newton's law combined with the Kirchhoof's law for the DC motor was considered.

$$J\frac{d^2\theta}{dt^2} + \beta\frac{d\theta}{dt} + C_o = k_m i, \tag{4.9}$$

$$L\frac{di}{dt} + Ri = V - k_e\frac{d\theta}{dt}. \tag{4.10}$$

Now, by using the Laplace transform, Eq. 4.4 and Eq. 4.4 can be written as:

$$Js^2\theta(s) + \beta s\theta(s) = k_m i(s), \tag{4.11}$$

$$Lsi(s) + Ri(s) = V(s) - k_e s\theta(s), \tag{4.12}$$

where s denotes the Laplace operator. Hence, the following block diagram for the DC motor can be construct,

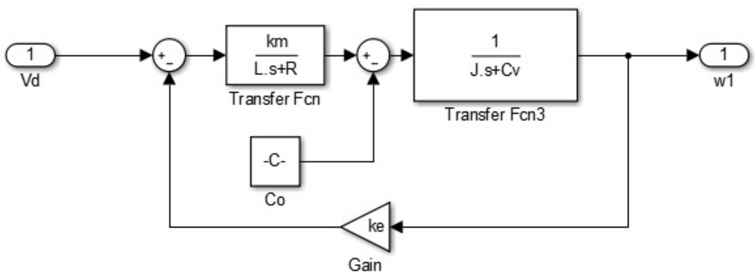

Figure 4.6: Simplified DC model

It was also verified that for the simplified DC motor model the output response are similar to the responses generated by the BLDC motor model. This model is going to be implemented in the preliminary

ADCS simulation, due to its simplicity and since there is no need to increase the simulation time in order to analyse the commutation process and observe the current flows.

4.5 Close-loop controller design

PID control is the most general form of feedback control. In the feedback vector of a BLDC controller often both the rotation speed and the current are included. The objective here is to decrease the costs of the launch by reducing the satellite's mass and also by decreasing the quantity of electronic material that should be used. Moreover, since the highly miniaturized drive electronics may leave no room space for components to measure the current, in order to suppress this problem the feedback vector contains only the rotation speed [23].

Selecting a motor with integrated sensors, in this case hall sensors, which will enable the system to determine the rotation speed of the motor is definitely one advantage to consider. Thus, the BLDC control consists of two elements [23]:

- **Commutation control**: As introduced commutation is actively executed by the drive electronics. Commutation control is required to ensure that the applied voltage is at all times applied over the proper set of stator electro coils for effective actuation of the motor.
- **Control available power**: In general it is not desirable for a motor to continuously deliver the maximum torque. Therefore, a PID controller shall be implemented over the input voltage to control the power available to the motor. This will also enable to control the velocity of the motor.

In this chapter it will be developed a controller to regulate the available power, which on its turn controls the torque of the motor. The commonly used PID control is implemented so that the supply voltage and thus the torque can be regulated. Using a typical representation of PID control the controlled voltage can be expressed as,

$$u(t) = K_p e(t) + K_i \int_0^t e(t)dt + K_d \frac{de(t)}{dt}, \tag{4.13}$$

where $u(t)$ is the voltage that is applied over the motor, e is the rotation speed error, K_p is the proportional gain, K_i is the integral gain and K_d is the derivative gain. e can be expressed in terms of the instantaneous rotation speed n and a reference rotation speed n_{ref} using the relation

$$e = n_{ref} - n. \tag{4.14}$$

The biggest issue to define the parameters and the gains of the PID controller relates to the fact that sometimes the searching for a simplified transfer function that could modulate the system can not be so transversally known. In this case it is important to make use of non-parametric techniques in order to tune the system response to a specific input.

There are several non-parametric techniques that can be used in order to tune the PID. One of the most old and used methods was developed by Ziegler and Nichols and published in 1942, and is widely used by controller manufacturers and process industry. The method is based on the determination of some features of process dynamics [46]. The controller parameters are then expressed in terms of the features by some simple formulas [47].

The determination of this parameters were based on the step-by-step response method [46]. It was verified after applied this method and also by using manual tuning for corrections that, $K_p = 9.7$; $K_i = 0.67$ and $K_d = 0.4$. This gains provided the desired responses for the RWS computational model, with a transient phase taking less than $3\ s$. The following figure, Fig. 4.7, represents the Simulink scheme of the close-loop model for this actuator that is going to be implemented in future simulations of the RWS.

Here the torque input vector $[1 \times 1]$, T_i, corresponds to the torque one shall generate around the z-axis direction w.r.t the fixed-body motor reference frame. This torque is then converted into the desired angular velocity of the wheel. The input parameters of the PID control corresponds to the desired velocity that was integrated from the desired torque, as well as the feedback angular velocity variable, w_1. Moreover, the system shall start with a nominal velocity of 18400 rpm, which is also an input parameter of the PID control, generated by a step block, whose step time variable is $t = 0\ s$.

After the PID control block a saturation block was implemented, in order to prevent the motor from damage, by avoiding voltage overload.

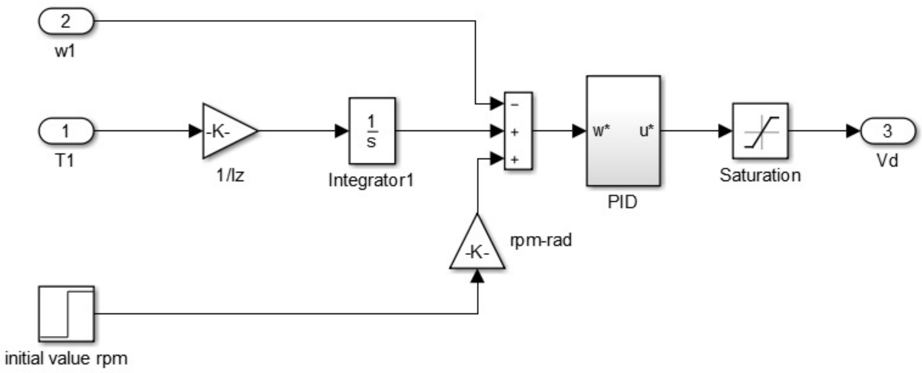

Figure 4.7: PID simulink block

It will be further explored in the overall system, but adding a low-pass filter to the system was necessary in order to reduce the noise generated by the time-derivative block used to determine the torque from the angular speed. It was observed that a simple second order low-pass filter with a low pass band frequency of $2.4\ rad/s$ would be enough in order to get the desired results, without increasing the transient step time delivered by the actuator. The parameters of the low-pass filter, namely the low-pass band frequency were determined by using manual tuning of the response.

As previously mentioned the nominal rotational speed of each wheel shall be $18400\ rpm$, which implies that in the beginning of the simulation, torques bigger than the ones expected for a pre-determined orbital manoeuvre may exist. The same shall occur in the real system. For the aforementioned RWS it shall be possible to simulate the start of this initial phase, when the system is switch on, and determine how it will affect the satellite, before the stabilization of the system in its nominal velocity.

The filtered results for the torque generated by one of the wheels in the Z-axis direction w.r.t the body-fixed motor reference frame are presented in Fig.4.8. As observed in Fig. 4.8 it takes approximately $20\ s$ for the torque delivered by each motor to stabilized after it was switch on.

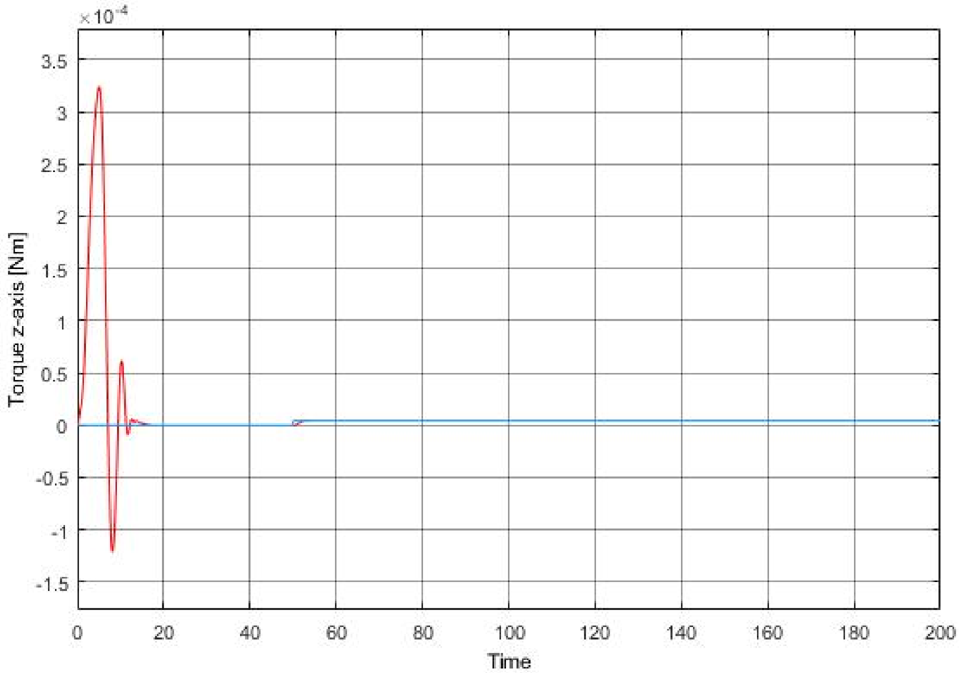

Figure 4.8: Torque generated in the Z-axis direction w.r.t the body fixed motor reference frame

This initial oscillation on the torque delivered is caused by the initial stabilization on the velocity of the wheel, since after the switch on of the motor it shall acquire a nominal angular velocity of $18400\ rpm$, which may take some time until it reaches the stable state. During that time there is an oscillatory torque which generates a torque magnitude two orders bigger than the torque needed to be provided by each motor in the axial direction in order to control the satellite during its manoeuvres.

Intuitively, this could lead to an unpredictable effected on the initial attitude of the spacecraft. However, the way how the pyramid configuration is rearranged as it will be seen, will neutralized this oscillatory torques right after the switch on of the system. Thus, it shall be expected a negligible effect on the satellite caused by this initial torque.

4.6 Overall system simulation

In the previous section it has been shown the response of an individual motor. Nevertheless, as it was presented in Chapter. 2, the RWS is going to be composed by four independent motors rearranged on a pyramidal configuration.

Based on the assumptions previously described it is now possible to create a valid model of the overall system. This actuator will have an input a $[3 \times 1]$ vector, which corresponds to the required torque that shall be applied to each axis in the satellite's body-fixed reference frame, T_{in}. The variable T_{out} is a

$[3 \times 1]$ vector which corresponds to the real torque delivered by the actuator to the satellite.

A schematic representation of the RWS model can be seen in Fig. 4.9. Inside each RW block there is the overall model of the each motor and respective flywheel. Both matlab functions are responsible to convert torque vector, T_{in}, in the torque each wheel should delivered.

The transformation from the wheel body frame is given by the $3 \times n$ distribution matrix W, already mentioned. This means that in MATLAB Function1 a pseudo-inverse of the mentioned matrix shall be used, in order to determine the torque vector of the wheel array.

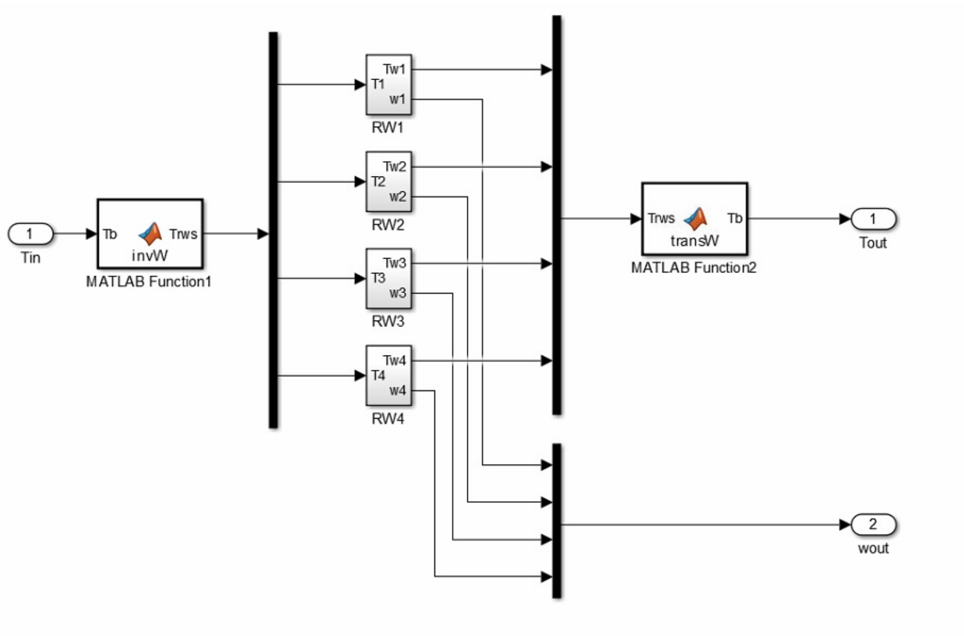

Figure 4.9: Overall RWS simulink block

In order to test and verify the behaviour of the actuator to the input responses a simulation analysis was performed. Accordingly to the satellite requirements and to the calculations already performed the minimum torque that shall be delivered around the y-axis of the satellite w.r.t. the body reference frame above Victoria shall be $T_y = 6.8 \times 10^{-6}$ Nm. It is difficult to estimate which torque is necessary to apply to the X and Y-axis, since only the upper bound of the perturbation torques caused by external factors were defined. Thus, it is going to be conjectured that the necessary torque needed will have a magnitude similar to the upper bound torques defined by the external perturbation forces. In sum, it will be assumed for the simulation a constant value of $T_x = T_z = 2.33 \times 10^{-6}$ Nm will be considered.

In this simulation to have more realistic results the update rate of the actuator variables will have a step size of 0.1 s, which will be the update rate of the real system to be implemented in ECOSat-III.

The results obtained for the torque delivered by the actuator to the y-axis w.r.t. the satellite's fixed-body reference frame to the aforementioned input step at $t = 50$ s can be consulted in Fig. 4.10. The input step is performed at $t = 50$ s in order to assure that each wheel was already rotating at its nominal speed by the time the step input was imposed.

This results were obtained without the implementation of the low-pass filter already mentioned, in order to see how the noise generated by the derivative block will affect the response of the overall system.

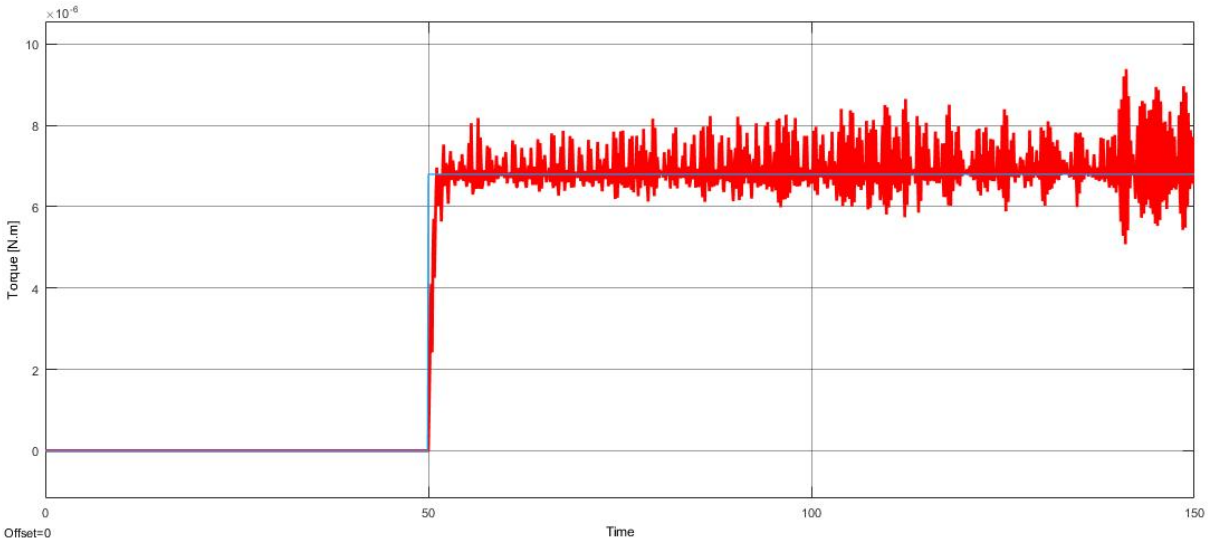

Figure 4.10: Torque generated in the Y-axis direction by the overall RWS w.r.t. the satellite's body-fixed reference frame - filter off

It is also possible to verify that the initial oscillatory torque produced by each motor was suppress when considered the overall system, as it was expected due to the creation of a null space torque vector caused by the way how the spin axis of each wheel are oriented in the pyramid configuration. Moreover, based on the results obtained it is possible to conclude that for a torque magnitude in the order of 10^{-6} Nm the noise generated will not have a negligible impact in the obtained response. This justifies why the use of a low-pass filter is important in order to obtain more accurate results. After applied the filter to the RWS, the following results were obtained, see Fig. 4.11

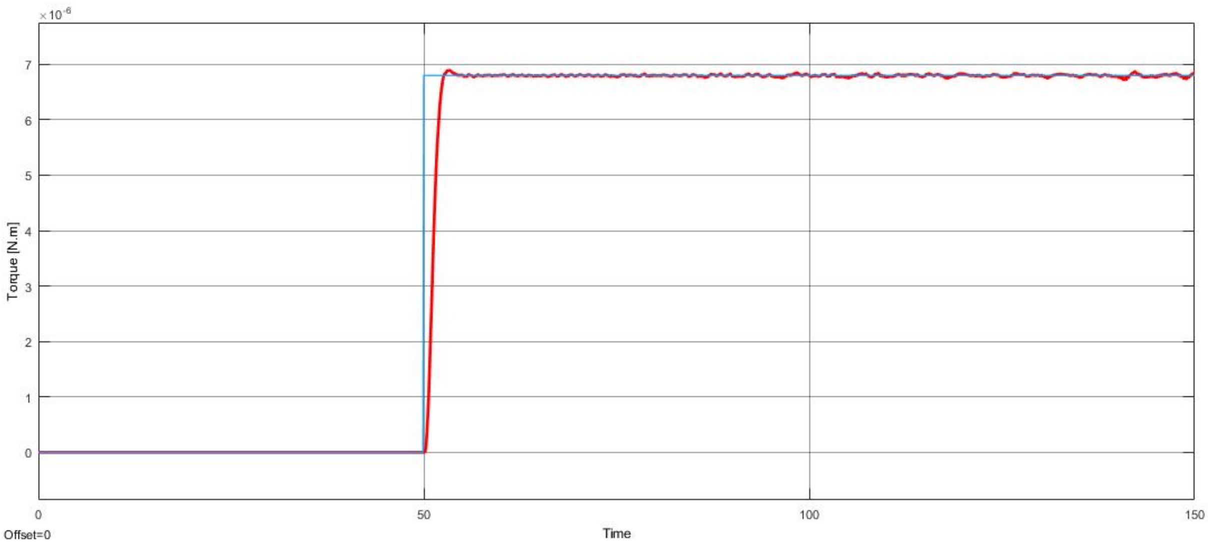

Figure 4.11: Torque generated in the Y-axis direction by the overall RWS w.r.t. the satellite's body-fixed reference frame - filter on

It is also important to determine and verify the changes in the rotational speed for each wheel. The following Fig. 4.12 shows how the rotational speed of each will evolve during the aforementioned manoeuvre.

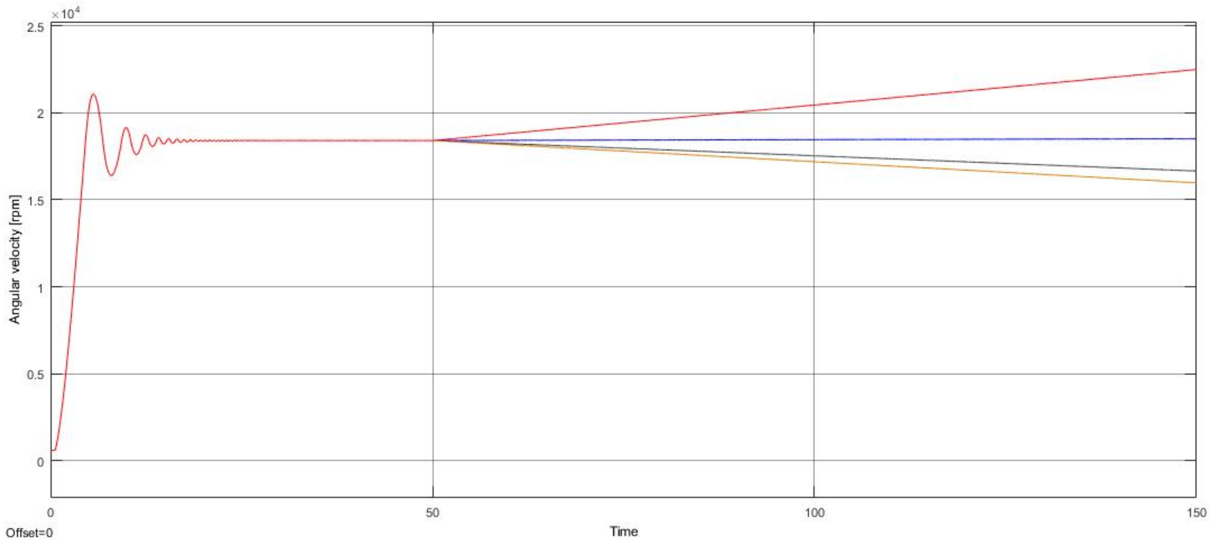

Figure 4.12: Angular velocity of each wheel [rpm] as function of the simulation time. (Brown - RWA $\#1$; Red - RWA $\#2$; Green - RWA $\#3$; Blue - RWA $\#4$

It is noted an harmonic oscillation around the nominal rotation speed of each wheel in the beginning of the simulation, which is caused by the switch on of the system. This oscillation will produced an undesired initial torque. However, as already explained it will be suppress due to the arrangement of the spin axis of each wheel.

4.7 Saturation of the RWS

The saturation of the RWS is one of the major concerns that should be taken into consideration. The rapid saturation of the RWS using the standard NASA configuration already mentioned in Chapter.2.3 was one of the reasons that led one to choose the pyramid configuration for the arrangement of the RWS, which ensures a bigger time until saturation, as well as guaranties the redundancy of the system. The mean time to saturation will determine the viability of the RWS, since if the RWS saturates in a very narrow time, there is a constant need to use the magnetorquers to desaturate the RWS. This will have major implications on the pointing precision, since magnetorquers have reduced pointing when compared to reaction wheels.

The RWS is projected based on the maximum torque that should be provided by the system. Each main manoeuvre above Victoria, B.C, takes approximately 400 s to complete. This means that the RWS should be operational and outside the saturation limits in order to guaranty the maximum pointing precision, for at least during this time. It is advisable to proceed to the desaturation of the wheel before this manoeuvre, as well as to start the manoeuvre above Victoria with the wheels rotating at its nominal speed, in order to increase the speed range available and prevent saturation.

Along this section a deeper study of the mean time to saturation is going to be considered, not only in the normal conditions, but also assuming that one of the wheels fail.

The results here presented are going to focus on the mean time this system takes to saturate, assuming that after the saturation of the first wheel, all the other wheels continue to provide exactly the same torque previously delivered,ı.e. each wheel will not increase the delivered torque in order to maintain the torque vector provided by the RWS.

Thus, after the failure of the first wheel it should be expected a decrease in the magnitude of the torque vector generated by the RWS.

4.7.1 Mean time to saturation - normal conditions

In normal conditions, ı.e if all the wheels are operational, for the manoeuvre already specified the RWS will entered into saturation only after $580\ s$, as it can be seen in Fig. 4.13.

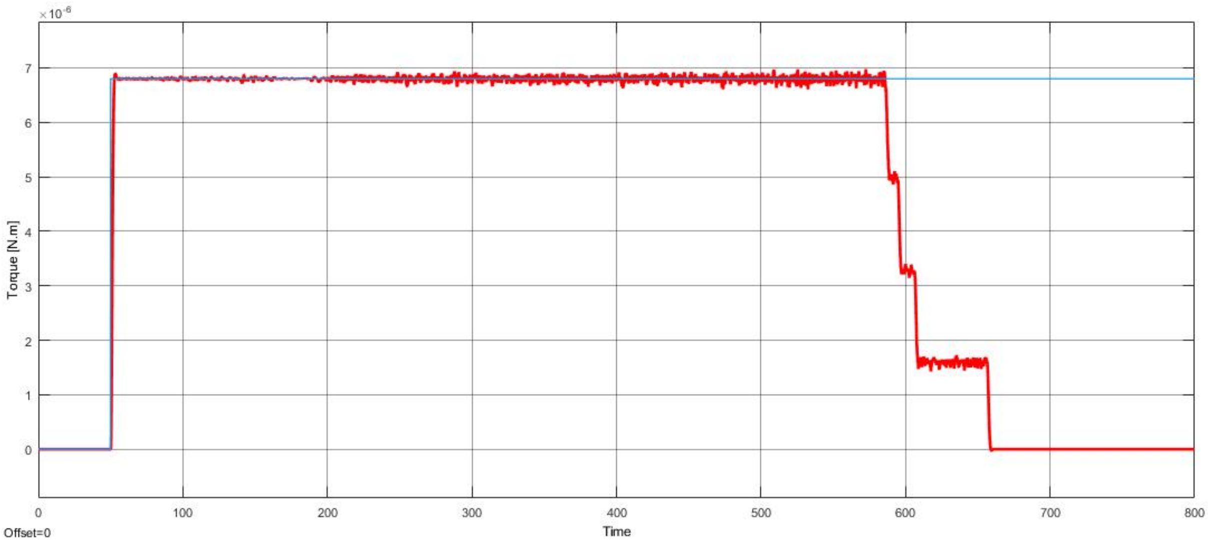

Figure 4.13: Torque generated in the Y-axis direction by the overall RWS w.r.t. the satellite's body-fixed reference frame in normal conditions until saturation

Thus, as expected for normal conditions the time it takes for the system to enter into saturation are inside the limits, ı.e. above 400 s. This guarantee that the mission objectives and requirements are fulfil, specially the ones related with the pointing position accuracy because there will be no need to use the magnetorquers which have reduced precision during this manoeuvre.

4.7.2 Mean time to saturation - failure of one wheel

It is also important to verify if the system takes more than 400 s to reach saturation during the aforementioned manoeuvre case one of the wheels fail. Considering the failure of the wheel number $\#1$, Fig. 4.14 is obtained.

The initial oscillating torque presented in the beginning of the simulation is related to the fact that the wheel failure was considered exactly after the switch on of the system. These torques in this case can not be cancelled, since it is impossible to generate a null total torque vector.

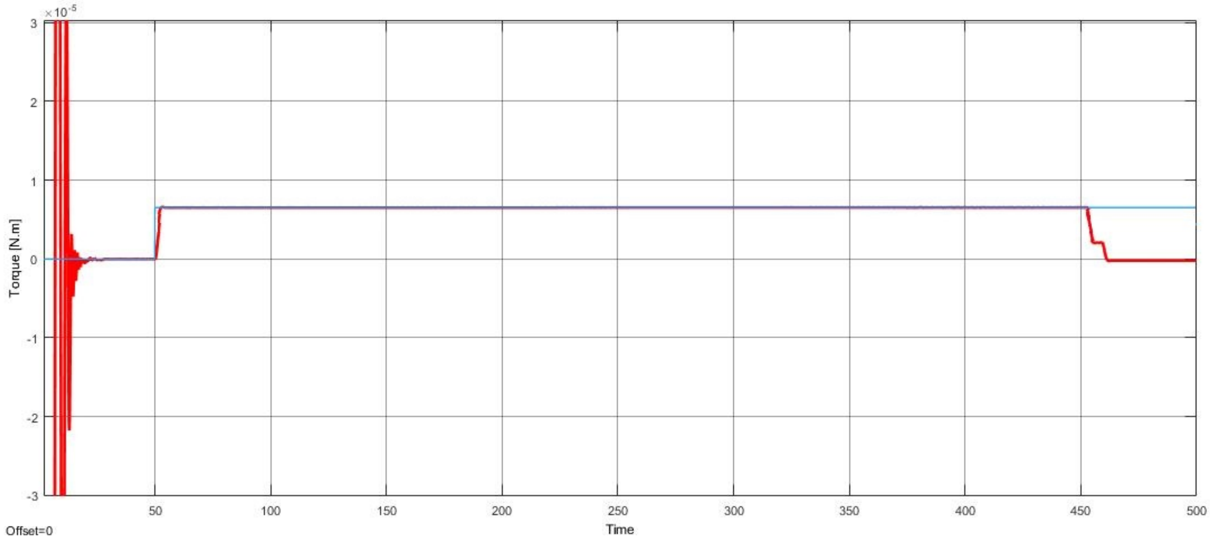

Figure 4.14: Torque generated in the Y-axis direction by the overall RWS w.r.t. the satellite's body-fixed reference frame assuming wheel $\#1$ has failed until saturation

Exactly, as in the normal conditions, one shall assume that a constant torque will be required during the orbital manoeuvre above Victoria. That step was defined at $t = 50\ s$. As observed in Fig. 4.14, the system will take approximately $400\ s$ to reach saturation, which is in the boundary of the defined limit. Nevertheless, this will not derail the RWS project, since this graphs were generated assuming worst case conditions. This means that the pointing precision shall not be affected, neither if one of the wheels fail.

Chapter 5

Mean life estimation

5.1 Mean time to failure

There are several space environmental factors that can cause the failure of a satellite. For instance, the use of electronic components which can be doped by solar radiation; the impact of micrometeorites; the failure of the propulsion system and software malfunction are examples of the causes that can induce a total failure of the satellite. However, the main contributor to satellite failures with 20% of the total satellite failures in the last 15 years is the RWS [48]. Thus, make a life estimation and increase the durability of this system is essential for the mission's success.

5.1.1 Basic Rating Life

There are several factors that can determine if the RWS is going to fail or not. Nevertheless, the reliability and the mean time to failure, MTTF, of this system is largely dependent on the bearing characteristics and lubrication of the motor.

Bearing life is an important factor to determine the survivability of the satellite under normal conditions [48, 49]. There are a number of factors involved in the life of the bearings, including the amount of bearing load the ball bearing is expected to handle. On Earth it is important to know the bearing life of the ball bearings in order to plane in advance when the replace of the bearing should be performed. However, in harsh space conditions and more precisely on ECOSat's mission it is impossible to substitute the bearing in case of failure. Thus, a rigorous analysis on the MTTF of the bearing should be performed.

According to ISO 281:2007 [50], for an individual bearing, or a group of apparently identical bearings operating under the same conditions, the life expectancy associated with 90% reliability, with contemporary, commonly used material and manufacturing quality, and under conventional operating conditions is given by,

$$L_{10} = \left(\frac{C_r}{P_r}\right) \times \frac{10^6}{n \times 60 \times 24 \times 365}, \tag{5.1}$$

where, L_{10} is the bearing life expectancy [years]; C_r is the basic dynamic radial load rating [N]; P_r is the dynamic equivalent radial load [N] and n corresponds to the rotational speed of the motor [rpm].

Dynamic equivalent radial load, P_r

Bearings subjected to primarily dynamic radial loads are usually subject to some axial forces. To interpret this combined radial and axial load it is convenient to consider a hypothetical load with a constant magnitude passing through the center of the bearing, P_r, see Eq.5.1.1

$$P_r = XF_r + YF_a, \tag{5.2}$$

where, $F_a = 1$ N is the radial load and $F_r = 0.6$ N is the radial load.

Compute the values for X and Y, see Tab.5.1, depends on the ratio F_a/F_r; on the number of rolling elements in a single row bearings, $Z = 6$; and on the nominal diameter of the ball bearing, $D_w = 1$ mm. The presented values for this parameters are specific for the selected motor (FAULHABER 1202BH004)

<table>
<tr><th></th><th></th><th colspan="2">$\frac{F_a}{F_r} \leq e$</th><th colspan="2">$\frac{F_a}{F_r} \geq e$</th></tr>
<tr><th>$\frac{F_a}{ZD_w}$</th><th>e</th><th>X</th><th>Y</th><th>X</th><th>Y</th></tr>
<tr><td>0.172</td><td>0.19</td><td rowspan="8">1</td><td rowspan="8">0</td><td rowspan="8">0.56</td><td>2.30</td></tr>
<tr><td>0.345</td><td>0.22</td><td>1.99</td></tr>
<tr><td>0.689</td><td>0.26</td><td>1.71</td></tr>
<tr><td>1.03</td><td>0.28</td><td>1.55</td></tr>
<tr><td>1.38</td><td>0.30</td><td>1.45</td></tr>
<tr><td>2.07</td><td>0.34</td><td>1.31</td></tr>
<tr><td>3.45</td><td>0.38</td><td>1.15</td></tr>
<tr><td>5.17</td><td>0.42</td><td>1.04</td></tr>
</table>

Table 5.1: Value for factors X and Y [50]

Based on the aforementioned table it was possible to conclude that $X = 0.56$ and $Y =$, which implies that $P_r = 2.636$ N

Basic Dynamic Radial Load Rating, C_r

It is defined as the constant radial load that a group of apparently identical bearings will theoretically endure for a rating life of one million revolutions. The calculation of the basic dynamic radial load rating is computed accordingly to ISO 281:2007 [50].

$$C_r = b_m f_c (icos\alpha)^{0.7} Z^{2/3} D_w^{1.8}, \tag{5.3}$$

where b_m is the rating factor depending on normal material and manufacture quality, which as a value of 1.3 for radial and angular contact ball bearings [50]; i is the number of rows of rolling elements in one bearing, which is 1 for the selected motor; α is the nominal contact angle [°] and its value was provided by the manufacturer as $\alpha = 12°$ and f_c is a coefficient dependent on the shape, processing accuracy and material of the bearing parts, which can be determined based on the following table that shows the values of f_c for a single row radial bearing,

$\frac{D_w cos\alpha}{D_{pw}}$	f_c
0.10	55.5
0.11	56.6
0.12	57.5
0.13	58.2
0.14	58.8

Table 5.2: f_c value for radial ball bearings [50]

The value for the pitch circle diameter of the ball set, D_{pw}, was estimated since there was no available data with the desired information. It was assumed that $D_{pw} = 7.5$ mm, considering the mean diameter between the cover of the motor and the shaft. By considering the data aforementioned and accordingly to Tab.5.2, $f_c = 58.2$. Now, by solving Eq.5.1 it is possible to compute the value of the basic dynamic radial load rating which is $C_r = 246$ N.

5.1.2 Modified L_{10} formula

Taking into account that both of the aforementioned loads were computed the value for the MTTF, based on Eq. 5.1.1 can be easily calculated. Assuming that in the majority of the operational time each motor will rotate at its nominal speed, ı.e. at $n = 18400$ rpm the value for the basic rating life should be $L_{10} = 84.07$ years. Nevertheless, this result is based in a general-purpose equation that covers all types and qualities of bearing making no allowance for specific cases, which may lead to some unrealistic results as observed. Thus, a modified formula shall be used in order to take into consideration life adjustment factors for reliability (a_1), and operating conditions (a_2),

$$L'_{10} = a_1 a_2 L_{10}. \tag{5.4}$$

The life adjustment factor for the reliability, a_1, recommended by the standards is given below,

Reliability (%)	a_1
90	1.00
95	0.62
96	0.53
97	0.44
98	0.33
99	0.21

Table 5.3: Reliability factor [49]

It was decided that for a Cubesat, a reliability of 99% must be considered, since for space applications it is fundamental increase the reliability of the the system, due to the high cost of technology that is being used in this industry, as well as the impossibility of orbital maintenance in case of failure, specially for a CubeSat.

It is also extremely useful to add the operational conditions, a_2, in order to determine the bearing life time, which is not considered in the non-modified formula. The factor a_2 is designed to take into account the thickness of the EHD (Elasto Hydro Dynamic) film relative to the composite roughness of the balls and raceways, as well as the cleanliness of the bearings, balls, raceways [51] [49]. The value of a_2 is determined based on the oil film parameter (Λ), which is the ratio between the resultant oil film thickness and surface roughness, see Fig. 5.1.

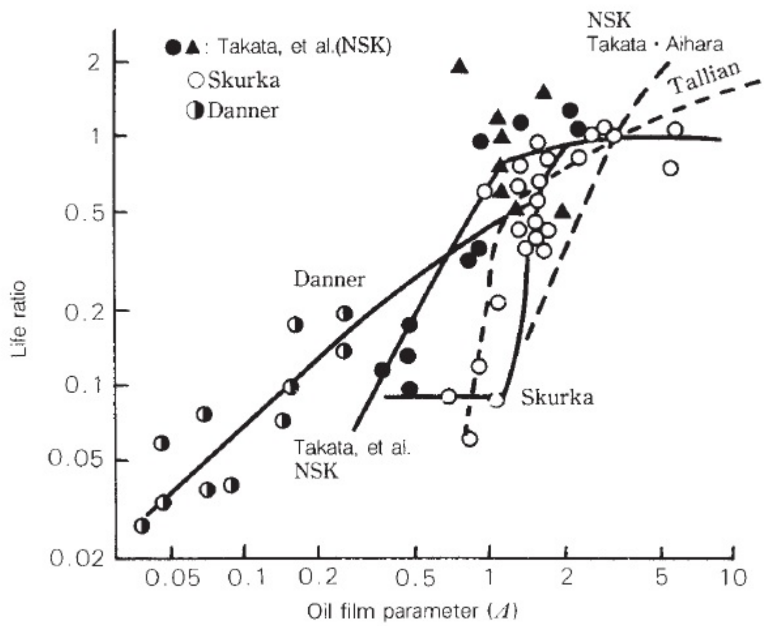

Figure 5.1: Typical experiment Λ and rolling fatigue life [51]

Thus, in order to determine a_2 it is strictly necessary to know the value of Λ, which can be obtained using the following equation [51],

$$\Lambda = T \cdot R \cdot A \cdot D, \tag{5.5}$$

where T is a factor dependent on the bearing type, which for a ball bearing as a value of 1.5 [51]; R is a factor related with the rotation speed; A is a factor related with the viscosity of the lubricant and D is related with the bearing dimensions.

Unfortunately there is not enough data available to determine the lubricant characteristics of the FAULHABER 1202BH004 motor, so several assumption are going to be made in order to compute the oil film parameter.

The first assumption relates to the type of lubricant that is included in the motor. One of the most common lubricants are the **esters** which were developed by the The British Petroleum in 1970 and after qualified by the European Space Tribology Laboratory (ESTL) for high speed mechanisms in the aerospace industry [52]. Moreover, the selected motor is highly recommended for aerospace applications. Thus, it should be coherent to assert that diester oil is the type of lubricant used in the selected motor.

There are several types of diester oil, however determine its viscosity is impossible based on the data provided by the FAULHABER company. Since, the objective is minimize the value of a_2 and consequently the value of Λ, it will be assumed the RWS motor will have the lowest viscosity for the diester oil, which is 1 mPa.s. This implies that A shall be 0.03, according to Fig. 5.2.

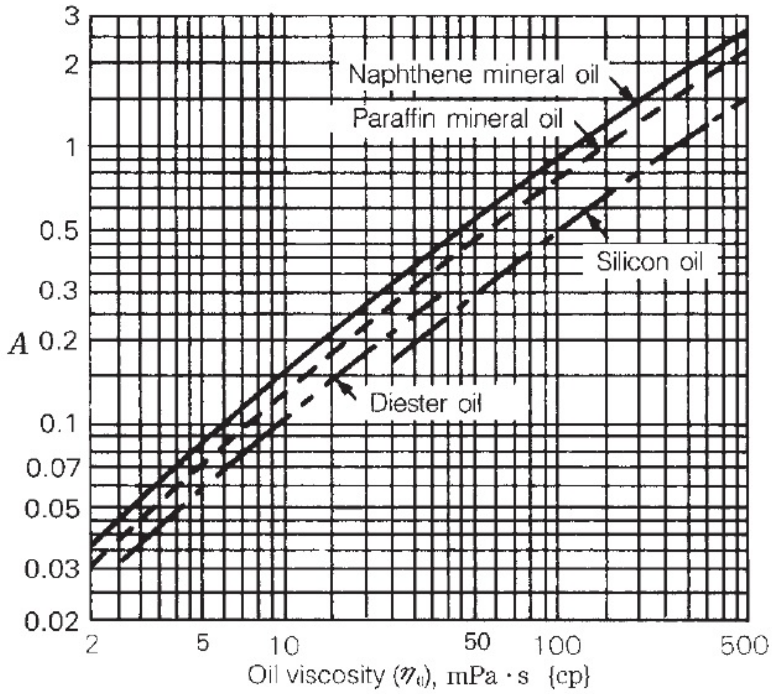

Figure 5.2: Term related to lubricant viscosity, A [51]

The second assumption relates to the diameter series of the bearing and also its bore diameter, d. As already explained the pitch diameter was computed based on the average value between the diameter of the shaft and the diameter of the cover. As a matter of simplification the bore diameter will be considered equal to the pitch diameter of the bearing, ı.e $d = 7.5$ mm.

Moreover, there is no data about the diameter series of the bearing. In order to minimize a_2 it will be assumed the diameter series of the bearing is 7.5. As it can be seen in Fig. 5.3, there is no data available for $d = 7.5mm$, which means the value of D will be based on an extrapolation outside the chart limits.

Hereupon, it will be assumed that the factor related with the bearing dimensions is $D = 0.18$.

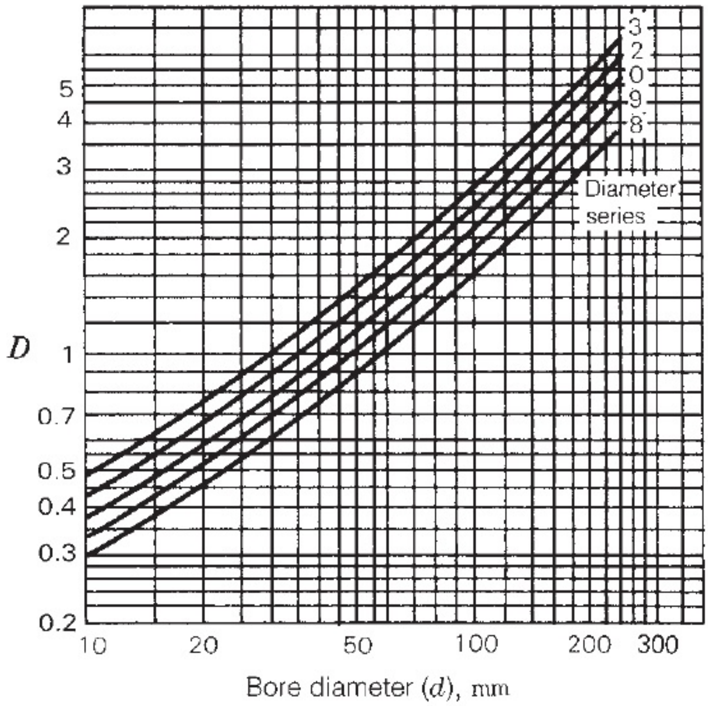

Figure 5.3: Term related to bearing specifications, D [51]

The last factor to determine is the one that relates to the rotational speed. By analysing Fig. 5.4 it is possible to conclude that for $n = 18400$ rpm, $R \simeq 25$.

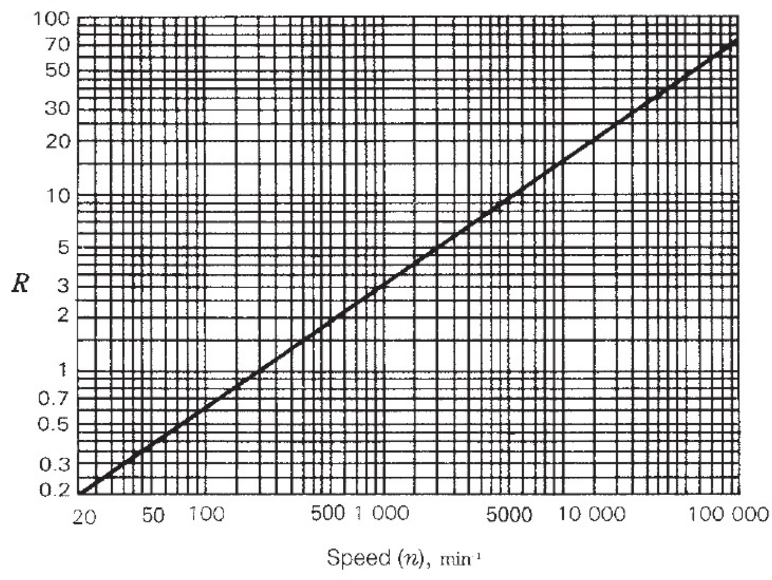

Figure 5.4: Term related to speed, R [51]

Then it is possible to determine the value of λ which is 0.28 and based on Fig. 5.1 it is concluded that $a_2 = 0.15$.

Thus, the MTTF using the modified L_{10} formula, see Eq.5.2, can now be updated. This alteration on the formula in order to give more realistic and reliable results as lower the basic rating life to $L'_{10} = 2.3$

years. The value for the basic rating life previously determined ensures that the satellite shall have success in its 2 years mission. Moreover, the use of four motors in a pyramidal configuration instead of three motors oriented according each axis in the body reference frame guaranties a redundant system, and consequently ensures qualitatively the increase of the life span of the RWS.

It is important to understand that the MTTF was determined based on the bearing failure of the motor, which is the main reason for the RWS failure, but not exclusively the only one. There are other factors which shall be taken into consideration, namely the fatigue caused on the system during the launch inside the rocked due to the micro-vibrations or the doping of electromechanical components responsible to control the torque delivered by the motor. These are only some examples of other factors that shall be considered in order to obtain a more reliable value for the MTTF of the RWS. Nevertheless, these other factors were neglected in this thesis, since there is yet any prototype available to perform such empirical tests. The change in the lubricant to a vacuum prove lubricant will also change the value in the MTTF. However, there is as yet no data available in order to determine the rate of change this modification will cause.

Notwithstanding considering other factors, in this Chapter it has been proven that under normal conditions with a reliability of 99% each motor should survive with no failure during a basic rating life of two and half years. This confirms once again that the RWS until now projected will be able to undertake the aforementioned space mission if only bearing failure is considered.

Chapter 6

Conclusions

In order to improve the pointing capabilities of CubeSats, a fast and precise response control system is required. Reaction wheels are an effective solution and rely on the simple principle of conservation of angular momentum, and they can also be developed within the stringent budgets of CubeSats supported by faculties and private institutions with current technologies.

The objective of the thesis was to develop a low-cost and reliable RWS for CubeSat applications, in particular to the ECOSat-III mission.

Firstly, an analysis of the requirements were made in order to determine the characteristics of the RWS, as well as to estimate the maximum torque that should be applied by the system, ignoring all the external perturbation forces, during ECOSat's principal manoeuvre. Next, the calculation of the perturbation torques enabled to determine the maximum torque expected to be delivered by the RWS during its orbital movement. This has allowed to define the upper bound for the expected torque to be delivered.

Next, the RWS design was presented. An comprehensive market research was done in order to determine all the available commertial solutions. The FAULHABER 1202 004 BH BLDC motor was selected due to its performance characteristics suitable for the proposed mission. The determination of the nominal speed of the motor, as well as the range of rotational velocities for each wheel was quantified.

Following the motor selection, an optimization of the disk-rim flywheel design was performed based on the minimization of its mass and radial stress. The process developed for the design of the flywheel can be applied to other industrial applications as well. The optimal RWS configuration to minimize the power consumption was also obtained. This analysis led to the conclusion that a pyramid configuration would be the best trade-off between the system's redundancy and its power consumption.

An extensive analysis of the torques caused by the internal disturbances, where the main sources are the axial play in the shaft of the motor and the flywheel manufacturing tolerances, has proved to have a negligible effect on the satellite reliability.

A new simplified model for a BLDC motor was also designed. The aforementioned model was the basis for the overall RWS model, which will be further implemented in the ADCS model already during the development phase. Nevertheless, for simplicity, in the first phase of the design process a common DC motor has been implemented in the ADCS of ECOSat-III.

The analysis based on a simulink model confirmed the viability of the system. It has been shown that a good and fast response for the desired input torques to be provided by each wheel is achievable. Moreover, the mean time until the system reaches the saturation is under the design limits, considering either the operation under normal conditions or assuming a failure of one wheel.

Finally, a MTTF analysis was performed in order to determine with a reliability of 99% if the future RWS would survive for at least during two years in space under nominal conditions.

In conclusion, it has been demonstrated that is possible to construct and develop a low-cost and reliable RWS to be implemented on a CubeSat.

Chapter 7

Recommendations and Future Work

The following research aspects should be considered and implemented in order to achieve the final RWS assembly:

a) Experimentally verify all the computational predictions in order to evaluate and validate the data obtained using the BLDC simulink model.

b) The design of the RWS assembly has not proven to be a trivial task. Thus, a joint collaboration between the faculty of Victoria and the FAULHABER Group would be very positive, in which it could be possible to optimize certain parameters for the specific use of the BLDC motor. An example relates to change of the lubricant into a high vacuum lubricant and the selection and construction of the brushless drive in order to minimize the noise generated and possibly the mechanical constant time.

c) It should also be developed an health monitoring system for each reaction wheel. Traditional diagnostics focus on detection of damage in order to identify components that will need replacement. Since bearing replacement is impossible in most spacecraft, the major objective here would be to detect potential problems early enough so that effective mitigation (e.g., the injection of additional lubricant) is possible prior to the occurrence of irreversible damage. The challenge is to identify the parameters that indicate the lubrication status before the bearing enters a damaging mode of operation. The use of cage temperature sensors has shown in previous studies that is highly effective for identifying the transition between EHL and mixed lubrication regimes [53]. Detection of this transition is the critical indicator that more lubrication is needed in order to prevent the damage. This would have improve the MTTF and increase the reliability of the system.

d) Special attention is needed in the area of space qualification. The materials that were suggested were feasible within those specifications for a space qualified product. The motor used, however is not vacuum proved and space qualifications tests shall be performed in order to guaranty its viability for a future launch. Moreover, further electronic components to use shall consider if the drive is space qualified or not. Furthermore, vibration tests shall be conducted, as well as vacuum and temperature tests, in order too assure the motor is qualified for space applications. These tests are also important in order to determine if some change to the preliminary design shall be conducted, namely in the arrangement of the RWS configuration or a change in the flywheel moment of inertia.

Bibliography

[1] E. Buchen and D. DePasquale. ”2014 - Nano and Microsatellite Market Assessment”. SpaceWorks Enterprises, Inc., 2014.

[2] M. Swartwout. ”Cubesat Design Specification R.12”. In *The Cubesat Program*. California Polytechnic State University, 2009.

[3] M. Swartwout. ”The First One Hundred CubeSats: A Statistical Look”. In *Journal of Small Satellites*, volume 2, pages 213–233. DeepakPublishing, 2013.

[4] J. Lousada. ”Design and development of the ECOSat’s Attitude Determination and Control System (ADCS) onboard software”. Master’s thesis, Instituto Superior Técnico, Lisboa, 2013.

[5] M. McLeod. ”UVIC engineering team wins satellite design challenge”, 2015. URL `http://www.design-engineering.com/general/uvic-engineering-team-wins-satellite-design-challenge-131765/`. from Design Engineering Online Magazine.

[6] EcoSat. ”ecoSat III”, 2015. URL `http://www.ecosat.ca/ecosat-iii/`.

[7] C. Husmann, P. Kazakoff, and A. Wulff. ”canadian satellite design challenge critical design review”. 2015. CSDC presentation.

[8] EcoSat. ”ecoSat II”, 2015. URL `http://www.ecosat.ca/ecosat-ii/`.

[9] ”Atittude Control Systems from CubeSatShop.com”, 2015. URL `http://www.cubesatshop.com/`.

[10] *”Small Spacecraft Technology State of the Art”*. NASA, 2014. Mission Design Division Staff, Ames Research Center, Moffett Field, California.

[11] S. Stoltz, F. Baumman, et al. ”RW-1 world smallest proved reaction wheel”. 2013. Astro- und Feinwerktechnik Adlershof GmbH, Berlin.

[12] S. Nodehin and U. Farooq. ”satellite atitude control using three reaction wheels”. *American Control Conference, Seattle*, 2008.

[13] H. Steyn. *”A multi-mode attitude determination and control system for small satellites”*. PhD thesis, Stellenbosch University, 1995. PhD Thesis.

[14] J. Wertz. *"Spacecraft Attitude Determination and Control"*. Reidel, 1978.

[15] A. Sabroff, J. Carrol, J. Clark, D. DeBra, et al. *"Spacecraft Gravitational Torques"*. NASA, Space Vehicle Design Criteria, May, 1969.

[16] R. Bohling, J. Carrol, J. Clark, D. DeBra, et al. *"Spacecraft Radiation Torques"*. NASA, Space Vehicle Design Criteria, May, 1969.

[17] J. Nocedal and S. J. Wright. *"Numerical optimization"*. Springer, 2^{nd} edition, 2006. ISBN:978-0387303031.

[18] J. Clark, D. DeBra, R. Bohling, J. Carrol, et al. *"Spacecraft Atmospheric Torques"*. NASA, Space Vehicle Design Criteria, May, 1969.

[19] R. A. Braeunig. "Rocket and Space Technology", 2015. URL `http://www.braeunig.us/space/atmos.htm`.

[20] D. Oltrogge and K. Leveque. "An Evaluation of Cubesat Orbital Decay". *AIAA/USU Conference on Small Satellites*, 2011.

[21] *"Applications of Aerospace Technology: Brushless DC Motors"*. NASA, Midwest Research Institute, January, 1975.

[22] M.V.Ramesh, J.Amarnath, et al. "Field Oriented Control for Space Vector Modulation based Brushless DC Motor drive". *International Journal of Advanced Research in Electrical, Electronics and Instrumentation Engineering IJAREEIE*.

[23] A. G. Hoevenaars. "Design, Integration and Verification of the Delfi-n3Xt Reaction Wheel System". Master's thesis, Delft University of Technology, Delft, 2012.

[24] "1202h006bh" product description, 2015. URL `http://www.micromo.com/1202h006bh.html`.

[25] S. Strener. "A unified approach for the analysis of rotating disks including turbine rotors". *International Journal of Solid and Structures*, (31):269–277, 1993.

[26] S. Jayaram. "design and analysis of nano momentum wheel for picosatellite attirude control system". *Aircraft Engineering and Aerospace Technology*, (81):424–431, 2009.

[27] L. You, H. Tang, and Y. Zhang. "numerical analysis of elastic-plastic rotating disks with arbitrary variable thickness and density". *International Journal of Solids and Structures*, (37), 2000.

[28] B. Bedier and I. Kholeif. "disk-rim flywheel with minimum weight". *Journal of American Science*, (7):146–149, 2011.

[29] A. Garza. "Reaction Wheels for Picosats". Master's thesis, Lulea University of Technology, Kiruna, 2009.

[30] K. Deb. *"Multi-objective optimization using evolutionary algorithms"*. John wiley and sons, 2nd edition, 2001. New York.

[31] A. Boresi and R. Schimidt. *"Advanced Mechanics of Materials"*. John Wiley and Sons, inc, 6^{th} edition, 2002. ISBN: 978-0-471-43881-6.

[32] H. Yoon, H. H. Seo, and H.-T. Choi. "Optimal uses of reaction wheels in pyramid configuration using new minimum finity-norm solution". *Aerospace Science and Technology, ELSEVIER*, 2014.

[33] A. Shirazi and M. Mirshams. "Pyramidal reaction wheel arrangement optimization of satellite attitude control subsystem for minimizing the power consuption". *International Journal of Aeronautical and Space Sciences*, 2014.

[34] P. Goel. "Auto Reconfiguration of Reaction Wheels in IRS". *IEEE Transactions on Aerospace and Electronic Systems*, (1):160–163, 1985.

[35] H. Kurokawa. "geometric study of single gimbal control moment gyros". Technical report, Mechanical Engineering Laboratory, Agency of Industrial Technology and Science, 1998.

[36] F. Markley and J. Crassidis. *"Fundaments of Spacecraft Attitude Determination and Control"*. Springer, Space Technology Labrary, 2014.

[37] A. Tashakori and N. Hosseinzadeh. "Modeling of BLDC Motor with Ideal Back-EMF for Automotice Applications". *Proceeding of the World Congress on Engineering, Vol II*, 2011.

[38] G. Prasad, N. Ramya, P. Prasad, and G. Tulasi. "Modelling and Simulation Analysis of the Brushless DC Motor by using MATLAB". *International Journal of Innovative Technology and Exploring Engineering (IJITEE), Vol.1, Issue-5*.

[39] Y. Jeon, H. Mok, et al. "A new simulation model of BLDC motor with real back EMF waveform". *IEEE on Computer and Power electronics*.

[40] S. Baldursson. "BLDC Motor Modelling and Control - a MATLAB/Simulink implementation". Master's thesis, Chalmers University of Technology, Gothenburg, Sweden, May 2005.

[41] M. Maru and D. Tanaka. "Consideration of Stribeck Diagram Parameters in the Investigation on Wear and Friction Behavior in Lubricated Sliding". *Journal of the Brazilian Society of Mechanical Sciences and Engineering, Vol.29, Rio de Janeiro*, March 2007.

[42] V. Geffen. "A study of friction models and friction compensation". December 2009. Traineeship report, Technische Universiteit Eindhoven, Department Mechanical Engineering, Dynamics and Control Technology Group.

[43] D. Rondão. "Modeling and Simulation of the ECOSat-III Attitude Determination and Control System". Master's thesis, Instituto Superior Técnico, Lisboa, 2016.

[44] D. Rai. "Simulink Simulator for a Brushless DC Motor", 2015. URL `http://www.mathworks.com/matlabcentral/fileexchange/12646-simulink-simulator-for-a-brushless-dc-motor`.

[45] D. Rai. *"Simulink Simulator for a Brushless DC Motor"*. Department of Electronics and Communication Engineering, National Institute of Technology Karnataka, India.

[46] K. Astrom and T. Hagglund. *"PID Controller: Theory, Design and Tuning"*. ISA, 1995.

[47] A. Schijndel. "pid - the basic technique for feedback control". Course notes from Control technology for building care systems, 7Y500 course from Technical University of Eindhoven.

[48] H. Li. "Reliability Modeling and Life Estimation Using an Expectation Maximization Based Wiener Degradation Model for Momentum Wheels". *IEEE Transactions on Cybernetics*, 45(5), May 2015.

[49] P. McMahon and R. Laven. "Results from 10 years of reaction/momentum wheel life testing". pages 21 – 23, September 2005.

[50] ISO. "rolling bearings – dynamic load ratings and rating life". ISO (ISO 281:2007), International Organization for Standardization, Geneva, Switzerland, 2007.

[51] NSK. "dynamic load rating, fatigue life, and static load rating". NSK e782g, 2015.

[52] H. Sathyan, H. Hsu, and S. Lee. "Long-term lubrication of momentum wheels used in spacecrafts — An overview". *ELSEVIER - Tribology International*, 43:259–267, May 2009.

[53] S. Marble and D. Tow. "Bearing Health Monitoring and Life Extension in Satellite Momentum/Reaction Wheels". *Aerospace Conference, IEEE*, 2006.

Appendix A

1202BH004 motor

Brushless Flat DC-Micromotors

0,16 mNm

For combination with
Drive Electronics:
Speed controller with adapter board

Series 1202 ... BH

	1202 H		004 BH	006 BH	
Nominal voltage	U_N		4	6	V
Terminal resistance, phase-phase	R		16	70	Ω
Output power [1]	$P_{2\,max.}$		0,652	0,492	W
Efficiency	$\eta_{max.}$		51	42	%
No-load speed	n_o		41 740	37 600	rpm
No-load current	I_o		0,028	0,015	A
Stall torque	M_H		0,222	0,124	mNm
Friction torque, static	C_o		0,003	0,003	mNm
Friction torque, dynamic	C_v		$0{,}52 \cdot 10^{-6}$	$0{,}52 \cdot 10^{-6}$	mNm/rpm
Speed constant	k_n		10 587	6 431	rpm/V
Back-EMF constant	k_E		0,094	0,156	mV/rpm
Torque constant	k_M		0,902	1,485	mNm/A
Current constant	k_I		1,109	0,673	A/mNm
Slope of n-M curve	$\Delta n/\Delta M$		187 793	303 121	rpm/mNm
Terminal inductance, phase-phase	L		26	58	µH
Mechanical time constant	τ_m		246	397	ms
Rotor inertia	J		0,125	0,125	gcm²
Angular acceleration	$\alpha_{max.}$		$18 \cdot 10^3$	$10 \cdot 10^3$	rad/s²
Thermal resistance	$R_{th\,1}$ / $R_{th\,2}$	0 / 94			K/W
Operating temperature range		-30 ... +85			°C
Shaft bearing		ball bearing			
Shaft load max.:					
– radial at 10 000 rpm (at shaft step ø3,4 mm)		0,6			N
– axial at 10 000 rpm (axial push-on only)		1			N
– axial at standstill (axial push-on only)		1			N
Shaft play:					
– radial	≤	0,011			mm
– axial	≤	0,060			mm
Number of pole pairs		4			
Weight		1,1			g
Direction of rotation		electronically reversible			

Recommended values - mathematically independent of each other					
Speed up to	$n_{e\,max.}$		40 000	40 000	rpm
Torque up to [2] [3]	$M_{e\,max.}$		0,16	0,12	mNm
Thermal current up to [3] [4]	$I_{e\,max.}$		0,199	0,095	A

[1] at 40 000 rpm [2] at 10 000 rpm [3] thermal resistance $R_{th\,2}$ not reduced [4] at standstill

Scale enlarged

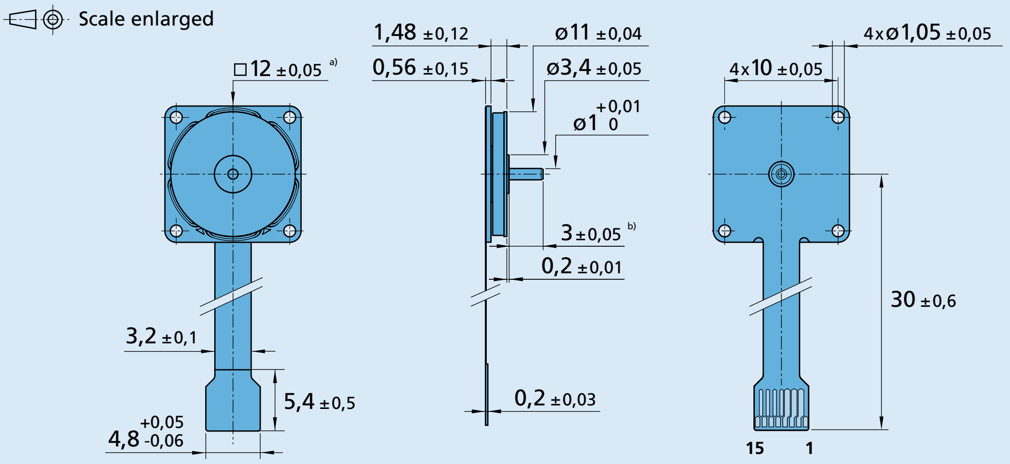

[a] also available with round stator ø12 ± 0,05
[b] also available with 1 mm output shaft length

1202 H ... BH

Connection

No.	Function
1	Star point
2	Phase A
3	Phase A
4	Phase B
5	Phase B
6	Phase C
7	Phase C
8	Hall sensor In +
9	Hall sensor In -
10	analog Hall A Out +
11	analog Hall A Out -
12	analog Hall B Out +
13	analog Hall B Out -
14	analog Hall C Out +
15	analog Hall C Out -

Connectors
15-pole; 0,3 mm pitch; e.g.:
Hirose: FH23-15S-0.3SHAW (05)

For notes on technical data and lifetime performance
refer to "Technical Information".
Edition 2014

Appendix B

Flywheel's blueprint

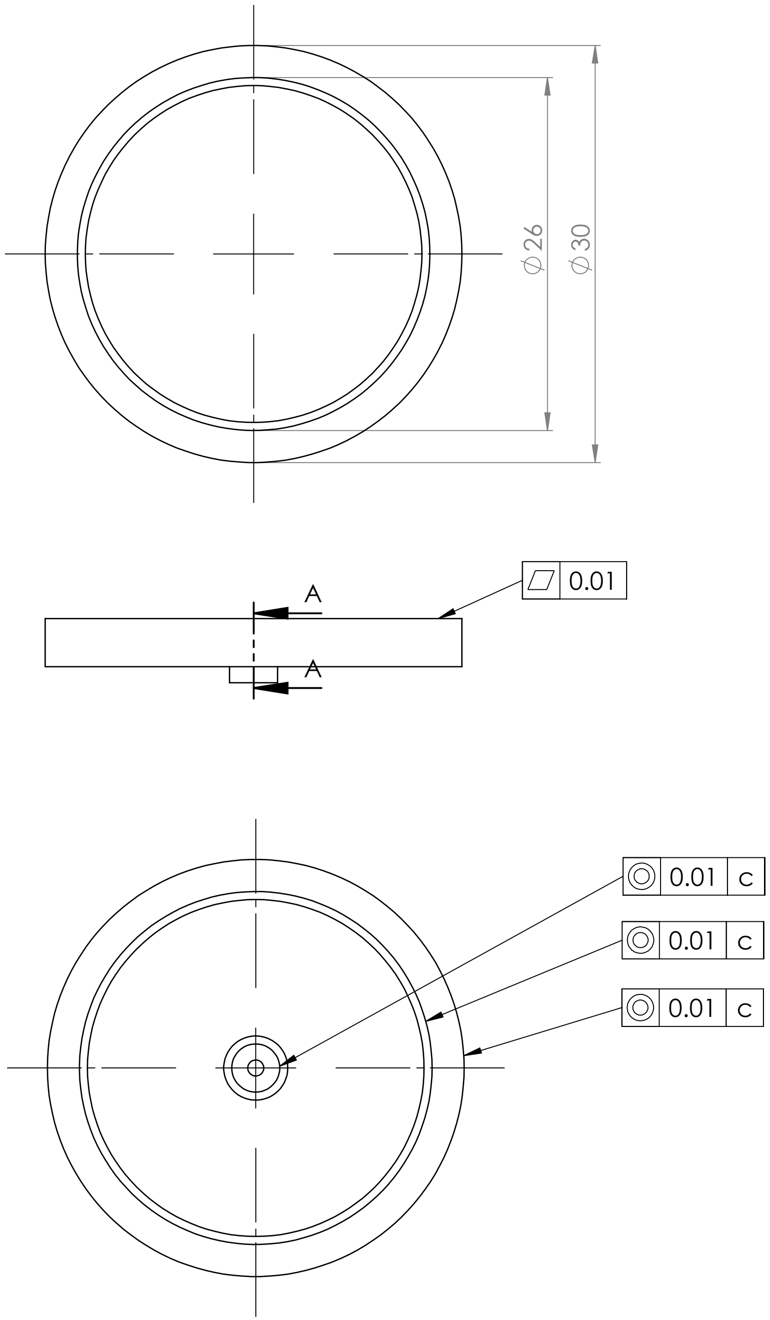

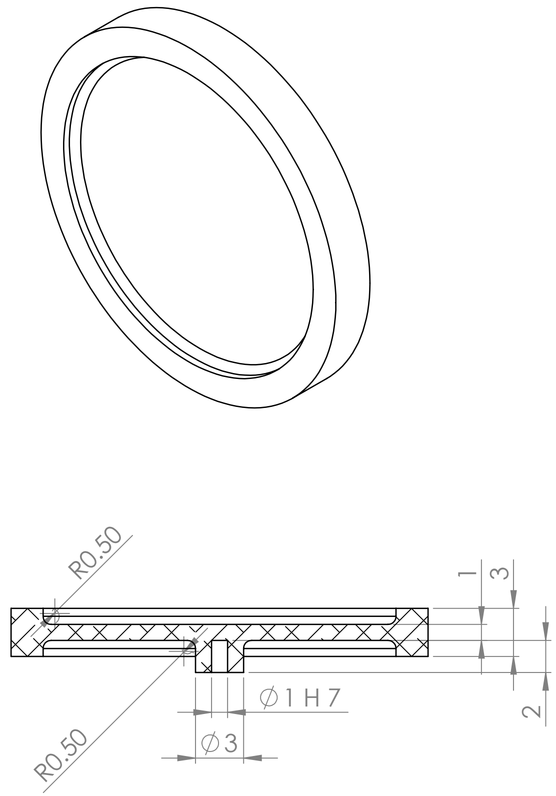

SECTION A-A

DIMENSIONS ARE IN MILLIMETERS
SURFACE ROUGHNESS: less than 1.6 micrometers
TOLERANCES: +/- 0.01 mm unless specified
ROUNDINGS: none, unless specified
REMOVE ALL SHARP EDGES

DEBURR AND BREAK SHARP EDGES

DO NOT SCALE DRAWING

REVISION

	NAME	SIGNATURE	DATE
DRAWN	Ricardo Gomes		10/07/2015
CHK'D			
APPV'D			
MFG			
Q.A			

TITLE:

RWS - Flywheel ECoSat-III project

MATERIAL:

Aluminium EN 2014

DWG NO.

Version 2.1

A3

WEIGHT: 3.85e-003 Kg

SCALE:5:1

SHEET 1 OF 1